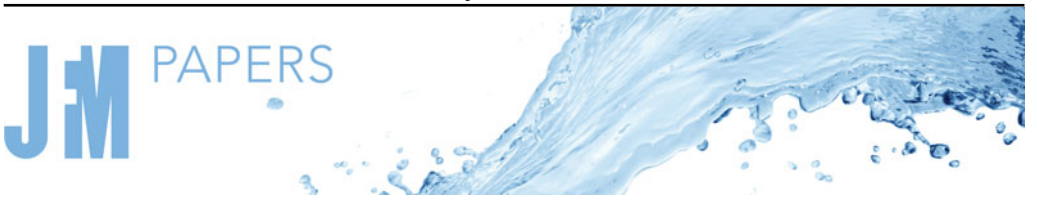
J. Fluid Mech. (2026), *vol.* 1033, A27, doi:10.1017/jfm.2026.11446



A systematic characterisation of canopy density based on turbulent-structure penetration

Zishen Chen[1] **and Ricardo García-Mayoral**[1]

[1]Department of Engineering, University of Cambridge, Trumpington Street, Cambridge CB2 1PZ, UK
Corresponding author: Ricardo García-Mayoral, r.gmayoral@eng.cam.ac.uk

(Received 24 June 2025; revised 14 March 2026; accepted 15 March 2026)

We investigate turbulent flows over canopies of rigid elements with different geometries, spacings and Reynolds numbers to identify and characterise different canopy density regimes. In the sparse regime, the overlying turbulence penetrates relatively unhindered within the canopy, whereas in the dense regime, this penetration is limited. The frontal density, λ_f, a common a measure of canopy density, is effective for e.g. conventional vegetation with no preferential orientation, but we observe that it does not fully characterise the density regime for some less conventional topologies, suggesting it may not always capture the underlying physics. To address this, we propose to quantify turbulence penetration directly, from the position and extent of individual turbulent eddies, particularly those associated with intense Reynolds shear stress. We analyse a series of direct simulations for isotropic- and anisotropic-layout canopies with frontal densities $\lambda_f \approx 0.01$–2.04, heights $h^+ \approx 44$–266, element width-to-pitch ratios $w/s \approx 0.06$–0.7 and Reynolds numbers $Re_\tau \approx 180$–2000. For the same λ_f, canopies with elements closely packed in the streamwise direction but large spanwise gaps result in deeper turbulence penetration, appearing sparser than isotropic or spanwise-packed ones. For the same spanwise gap, turbulence penetration remains similar across canopies independently of their streamwise pitch and gap. As the spanwise gap increases, eddies penetrate deeper and more vigorously into the canopy. Turbulence penetration is also Reynolds-number-dependent: the same canopy can behave as dense at low Re_τ, but increasingly sparse as Re_τ increases. Our results suggest that turbulence penetration depends essentially on the ability of turbulent eddies to fit within the canopy as they travel downstream, and that this can be characterised by an effective spanwise gap, and its ratio to the typical eddy size; turbulence penetration is substantial when this gap is larger than the eddy size, and negligible in the opposite case. A penetration length d_p can then be defined from the effective gap or the eddy size, whichever is smaller. For small d_p/h, the canopy behaves

© The Author(s), 2026. Published by Cambridge University Press. This is an Open Access article, distributed under the terms of the Creative Commons Attribution licence (https://creativecommons.org/licenses/by/4.0/), which permits unrestricted re-use, distribution and reproduction, provided the original article is properly cited.

https://doi.org/10.1017/jfm.2026.11446 Published online by Cambridge University Press

as dense; for moderate d_p/h, as intermediate; and for $d_p/h \approx 1$, turbulent eddies can penetrate all the way to the canopy bed and the canopy behaves as sparse.

Key words: turbulent boundary layers, turbulence simulation

1. Introduction and background

Canopies of protruding elements are ubiquitous in practical flows, holding significant environmental and engineering importance. Vegetation canopies are of great ecological importance to both terrestrial and aquatic ecosystems, mediating the concentration of nutrients, oxygen and carbon (Malhi 2002; Baldocchi 2003), as reviewed by Finnigan (2000), Belcher, Harman & Finnigan (2012), Nepf (2012*a*,*b*) and Brunet (2020). Canopies of pin-fin arrays are widely used in industrial applications for heat transfer enhancement (Ligrani, Oliveira & Blaskovich 2003; Peles *et al.* 2005; Arshad *et al.* 2017), as summarised in Mousa, Miljkovic & Nawaz (2021). The study of canopy turbulence is also relevant to a wide range of applications, including cooling urban heat islands (Akbari & Kolokotsa 2016; Rahman *et al.* 2020), mitigating agricultural loss due to windthrow (Berry *et al.* 2004; De Langre 2008), monitoring the transport of airborne pollutants (Belcher 2005; Escobedo, Kroeger & Wagner 2011; Janhäll 2015) and forecasting weather (Britter & Hanna 2003; Blocken 2015). Consequently, understanding the interaction between canopies and turbulence is crucial for effectively managing such practical flows and improving the related environmental and industrial practice.

Canopy density has a direct impact on the turbulent flow within and immediately above the canopy (Nepf 2012*a*; Brunet 2020; Sharma & García-Mayoral 2020*a*,*b*). Poggi *et al.* (2004) conducted experiments on flows over various canopy densities and identified the characteristics of different density regimes, suggesting that the flow over canopies can be broadly divided into three components. A graphical illustration of these components and their characteristic eddies for dense and sparse canopies is depicted in figure 1. The first component is the background turbulence characteristic of boundary layers – this is the component that would be present even in the absence of the canopy. The second component is the element-induced or element-coherent flow, which mainly occurs within the canopy and results from the obstruction caused by individual elements (Cava & Katul 2008; Dupont *et al.* 2011). The third component is the mixing-layer-like flow that forms due to the mean-flow inflection in the vicinity of the canopy-tip plane of a dense canopy (Raupach, Finnigan & Brunet 1996; Finnigan 2000; Finnigan, Shaw & Patton 2009). Poggi *et al.* (2004) emphasised that the flow behaviour near the canopy-tip plane is largely dependent on the canopy density regime, and that mixing-layer-like eddies only appear when the canopy density is high enough to induce a strong and relatively homogeneous shear layer (Raupach *et al.* 1996; Sharma & García-Mayoral 2020*b*). If we consider the eddies from the background turbulence as they penetrate into the canopy, their relative intensity and penetration depth vary depending on the canopy density (Nepf 2012*a*; Brunet 2020). As illustrated in figure 1(*a*), dense canopies with closely packed elements effectively limit the penetration of the background turbulence, and the flow within is essentially sheltered from that above, except for a weak footprint of the mixing-layer eddies (Sharma & García-Mayoral 2020*b*). In contrast, as depicted in figure 1(*b*), sparse canopies with large element spacing allow the background turbulence to penetrate relatively unhindered into the canopy. Based on this, turbulence over sparse canopies has typically been considered a simple superposition of the wall-bounded flow and the

https://doi.org/10.1017/jfm.2026.11446 Published online by Cambridge University Press

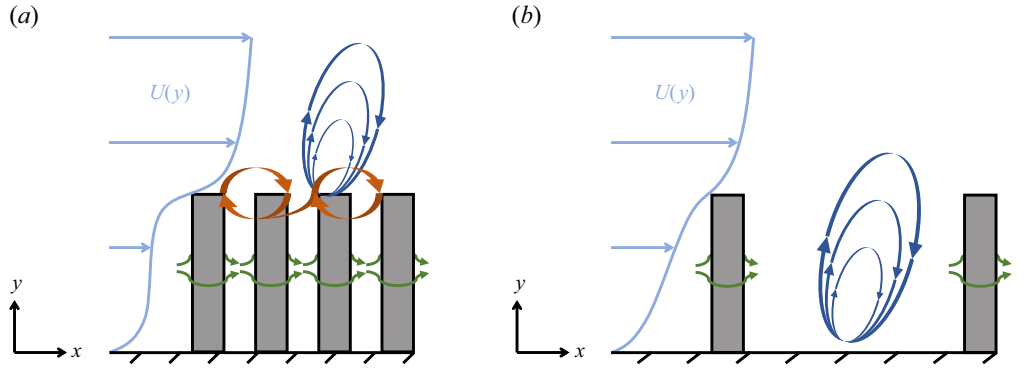


Figure 1. Graphical illustration of the flow regimes over (*a*) dense and (*b*) sparse canopies. The dark blue, orange and green arrows represent the background-turbulence eddies, mixing-layer-like eddies and element-coherent eddies, respectively. Adapted from Poggi *et al.* (2004) and Sharma (2020).

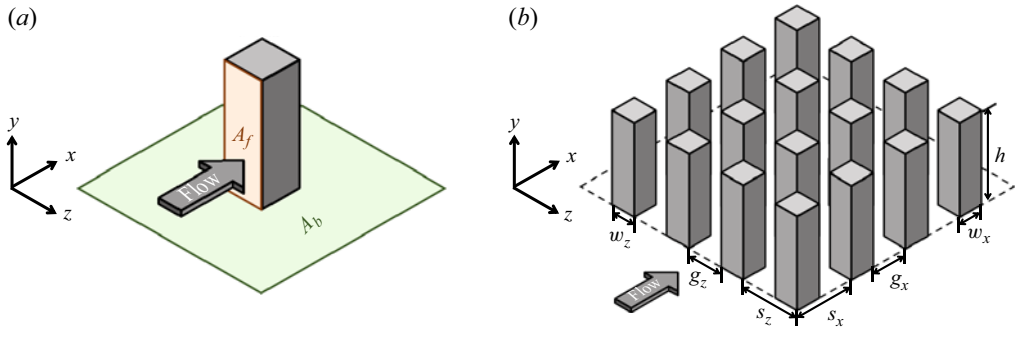


Figure 2. Schematic representation of (*a*) a canopy element and (*b*) a layout of canopy elements. In (*a*), A_f is the frontal area and A_b is the bed area occupied by each element. In (*b*), h is the element height, w_x, g_x and s_x are the element width, gap and spacing (pitch) in the streamwise direction, respectively, and w_z, g_z and s_z are those in the spanwise direction.

element-coherent flow, where the mean velocity profile resembles that over a smooth wall (Huang, Cassiani & Albertson 2009; Pietri *et al.* 2009; Nepf 2012*a*). However, this argument is valid only when the drag induced by the canopy elements is negligible compared with the total drag. Recent direct numerical simulations (DNSs) have shown that even canopies with a frontal density as low as $\lambda_f \approx 0.01$ and spacing-to-height ratios as large as $s/h \approx 4$ can result in substantial element-induced drag, accounting for more than 60 % of the total drag, and that such sparse canopies mainly modulate the background turbulence through their drag on the mean velocity profile, as the mean shear sets the scale of turbulence locally at each height (Sharma & García-Mayoral 2020*a*).

A popular quantity to characterise canopy density is the frontal density (Nepf 2012*a*), also known as the leaf area index in the vegetated-canopy literature (Wooding, Bradley & Marshall 1973; Kaimal & Finnigan 1994)

$$\lambda_f = \frac{A_f}{A_b} = \frac{1}{A_b}\int_0^h w_z(y)\mathrm{d}y, \tag{1.1}$$

where A_f/A_b indicates the frontal area per unit bed area, h is the element height and $w_z(y)$ is the element frontal width at each height y, as depicted in figure 2(*a*). For the present prismatic canopies, the frontal density becomes $\lambda_f = w_z h/(s_x s_z)$, as shown in figure 2(*b*),

https://doi.org/10.1017/jfm.2026.11446 Published online by Cambridge University Press

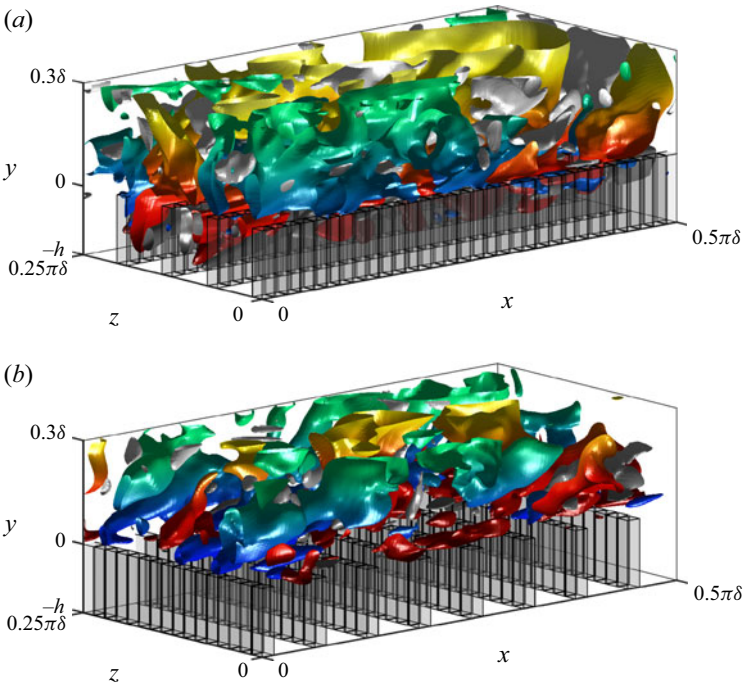


Figure 3. Instantaneous realisations of the $u'v'$ structures over and within canopies with the same number of elements per area and frontal density $\lambda_f \approx 0.91$: (*a*) streamwise-packed canopy $\mathrm{C_{S27\times108}}$ with $s_x^+ \approx 27$, $s_z^+ \approx 108$ and $h^+ \approx 110$, and (*b*) spanwise-packed canopy $\mathrm{F_{S108\times27}}$ with $s_x^+ \approx 108$, $s_z^+ \approx 27$ and $h^+ \approx 110$. The structures are coloured by distance to the floor, and consist of ejections ($u' < 0$, $v' > 0$ blue to green), sweeps ($u' > 0$, $v' < 0$ red to yellow) and outward and inward interactions ($u'v' > 0$ grey to white). Cases $\mathrm{C_{S27\times108}}$ and $\mathrm{F_{S108\times27}}$ are fully defined in table 1.

where w indicates the element width, g the gap between elements and s their pitch or spacing, with the subscripts referring to the streamwise (x) and spanwise (z) directions. Nepf (2012*a*) noted that canopies are dense when $\lambda_f \gg 0.1$, sparse when $\lambda_f \ll 0.1$ and intermediate between the two limits. Permeability and porosity (ϕ) are also popular measures of density for denser canopies and other permeable substrates, embodying the 'accessibility' of the fluid region (Breugem, Boersma & Uittenbogaard 2006; Lightbody & Nepf 2006; Luhar, Rominger & Nepf 2008). However, these geometric parameters only provide a notional measure of canopy density, and occasionally fail to capture how different element arrangements can result in different flow regimes. The studies by Pietri *et al.* (2009) and Bailey & Stoll (2013) highlighted that identical density values of λ_f and ϕ do not necessarily translate to similar flow penetration behaviours and may not accurately reflect the actual canopy density regime. This limitation is illustrated in figure 3, depicting structures of intense $u'v'$ over canopies with the same number of elements and identical λ_f but different element layouts, which are discussed in full detail in § 4.1. As shown in figure 3(*a*), these structures penetrate more effectively into the streamwise-packed canopy compared with the spanwise-packed canopy in figure 3(*b*), showing that element layout, a factor not captured by λ_f, can significantly influence the canopy density regime.

The frontal density λ_f has been proposed as a predictor for canopy density because it is a convenient surrogate for physics-based quantities, such as the drag length ℓ_d, which characterise the impedance that the canopy exerts on the flow (Nepf 2012*a*). The drag length ℓ_d gives a measure of how quickly the mean flow $U(y)$ decays below the canopy tips, and

https://doi.org/10.1017/jfm.2026.11446 Published online by Cambridge University Press

can be defined as $\ell_d = U^2/F_D$ using the mean velocity and surface drag F_D at the plane of the tips. It would then be natural to expect that the differences between streamwise- and spanwise-packed layouts mentioned above could be captured by parameters such as ℓ_d since, even for the same λ_f, the higher drag sheltering for streamwise-packed configurations results in a larger ℓ_d. Other length scales that can quantify the penetration of the mean flow are the shear length $\ell_s = U/(\mathrm{d}U/\mathrm{d}y)$ measured at the tip plane, which quantifies how inflexional the $U(y)$ profile is, and thus the intensity of the drag acting on it (Endrikat *et al.* 2021), or the depth below the tips of the zero-plane displacement, d_0, the depth perceived as the origin by the overlying turbulence (Chen & García-Mayoral 2023). All these length scales, however, characterise the effect of the canopy on the penetration of the mean velocity profile, rather than of the set of fluctuating eddies that conform the overlying turbulence. This paper will propose a length scale to characterise canopy density based on the latter. For conventional canopy layouts, such as x–z-isotropic vegetation canopies and their regular surrogates often studied in the literature, we would expect reasonable correlation between both approaches, but possibly not for counter-examples such as those of figure 3. An assessment of the above length scales as predictors for density can be found in Appendix A. They provide a generally correct trend but with significant scatter, comparable to that produced using the purely geometric λ_f.

Sharma & García-Mayoral (2020*a*) argued that a canopy would be sparse if the spanwise spacing between elements is $s_z^+ \gtrsim 100$, which is large enough to fit in the near-wall streaks of characteristic width $\lambda_z^+ \approx 100$ (Kline *et al.* 1967; Kim, Kline & Reynolds 1971). This is consistent with the observations of Poggi *et al.* (2004) and Huang *et al.* (2009), who noted a progressive departure from smooth-wall behaviour for sparse canopies as the spacing between elements decreases. However, Sharma & García-Mayoral (2020*a*) investigated only sparse canopies of isotropically laid filaments, and did not consider the effects of a wider variety of geometric parameters; a spanwise spacing can be easily defined for the collocated elements of Sharma & García-Mayoral (2020*a*), but doing so for irregular or even staggered arrangements may be less straightforward. Canopies that are clearly sparse or clearly dense were extensively investigated in Sharma & García-Mayoral (2020*a*) and Sharma & García-Mayoral (2020*b*), but the transition from one limit to the other was not directly considered. This highlights the need for a more systematic approach to measure the extent of turbulence penetration, and to characterise canopy density. Recent studies have proposed to characterise canopy density as determined by the interchange between the relative vertical positions of the zero-plane-displacement height and the inflection in the mean velocity profile that occurs within the canopy (see e.g. Monti *et al.* 2020, and follow-up papers). The latter inflection occurs due to the near-bed boundary layer that forms in order for the mean flow to satisfy no slip at the bed. The authors argued that this lower inflection played a key role in the flow dynamics, as it gave rise to an instability, reminiscent of Kelvin–Helmhotz, because the mean velocity profile satisfied Fjørtoft's criterion for instability. The opposite is unfortunately the case: Fjørtoft's criterion predicts instability for a mixing-layer type, concave-to-convex inflection, like the one at the canopy tips, and stability for convex-to-concave inflections like the one near the bed. Physically, the flow is the most unstable where the mean shear is maximum, and most stable where the shear is minimum. Furthermore, for flows in homogeneous canopies, the lower inflection can only occur when the flow is driven by a mean pressure gradient or a body force, when a Darcy-like region of uniform velocity tends to form in the canopy core, requiring a Brinkman-like boundary layer at its bottom to meet no slip at the bed. Beyond pressure gradients, inner inflections can also appear when there is a local maximum in the mean velocity profile within the canopy, which can be caused by inhomogeneities such as edge effects and differences between trunk and crown drag (see e.g. Dupont *et al.* 2011,

https://doi.org/10.1017/jfm.2026.11446 Published online by Cambridge University Press

and references therein). Otherwise, when the intra-canopy flow is driven mainly by the shear exerted by the overlying flow, as in zero-pressure-gradient boundary layers, the Darcy-flow contribution is non-existent, and there is therefore no inner inflection. A different approach is therefore necessary to characterise canopy density in a common framework across the broad flow typology.

In the present study, we conduct DNSs of canopies with different layouts and element geometries. We aim to establish a metric for canopy density based on the flow dynamics to enable the quantitative diagnosis, characterisation and prediction of canopy density. For this, we quantify the extent and depth of the penetrating three-dimensional turbulence structures of intense Reynolds shear stress $u'v'$ (Del Alamo *et al.* 2006; Lozano-Durán *et al.* 2012). We focus on these structures because they are responsible for momentum transport and turbulence diffusion between the overlying and the canopy regions, and are ultimately responsible for the wall-normal distribution of the Reynolds stress and thus the shape of the mean velocity profile. Based on this measure, we explore the influence of the different geometric characteristics of the canopy on whether turbulence penetrates or not, and identify which are the key ones to determine canopy density. The paper is organised as follows. § 2 presents the numerical method and the different canopies simulated. § 3 introduces and discusses the metrics used to measure turbulence penetration. § 4 presents the DNS results, focusing on how different canopy parameters affect turbulence penetration. Finally, § 5 summarises the conclusions of our investigation.

2. Methodology

In this section, we briefly discuss the DNS method in § 2.1, and present the relevant parameters for the canopies simulated, with different element geometries and layouts, in § 2.2.

2.1. *Direct numerical simulations*

We carry out DNS of doubly periodic closed symmetric channels with rigid filament canopies protruding from both walls. The coordinates x, y and z represent the streamwise, wall-normal and spanwise directions, respectively. The filament canopies and the numerical domain studied are portrayed in figure 4, where $\delta = 1$ is the channel half-height measured from the channel centre to the canopy-tip planes. The canopy elements extend below $y = 0$ on the bottom wall and above $y = 2\delta$ on the top wall. For all simulations the channel streamwise and spanwise dimensions are at least $L_x \times L_z = 2\pi\delta \times \pi\delta$, and up to $2.8\pi\delta \times 1.4\pi\delta$. Compared with open channels, closed channels entail roughly twice as much computational cost per time step, but they also produce twice as many statistical samples. The two set-ups are essentially equivalent for the near-wall flow. They can exhibit different properties in the wake region above the logarithmic layer, where turbulence activity is significantly inhibited by the no-transpiration boundary condition in open channels, while the centre of a closed channel allows eddies to flow freely, with a closer resemblance to boundary layers. For canopy flows we have reported these wake differences in Chen & García-Mayoral (2023), where they were confined to the top $\sim$20 % of the flow thickness, and they are examined in depth across different flows, including open and closed channels, Couette flow and boundary layers, in Luchini (2018, 2024).

The DNS code in this study is from Sharma & García-Mayoral (2020*a*,*b*) and has been validated in Sharma (2020) and Chen & García-Mayoral (2023). It is summarised here for reference. The numerical method resolves the three-dimensional incompressible Navier–Stokes equations,

https://doi.org/10.1017/jfm.2026.11446 Published online by Cambridge University Press

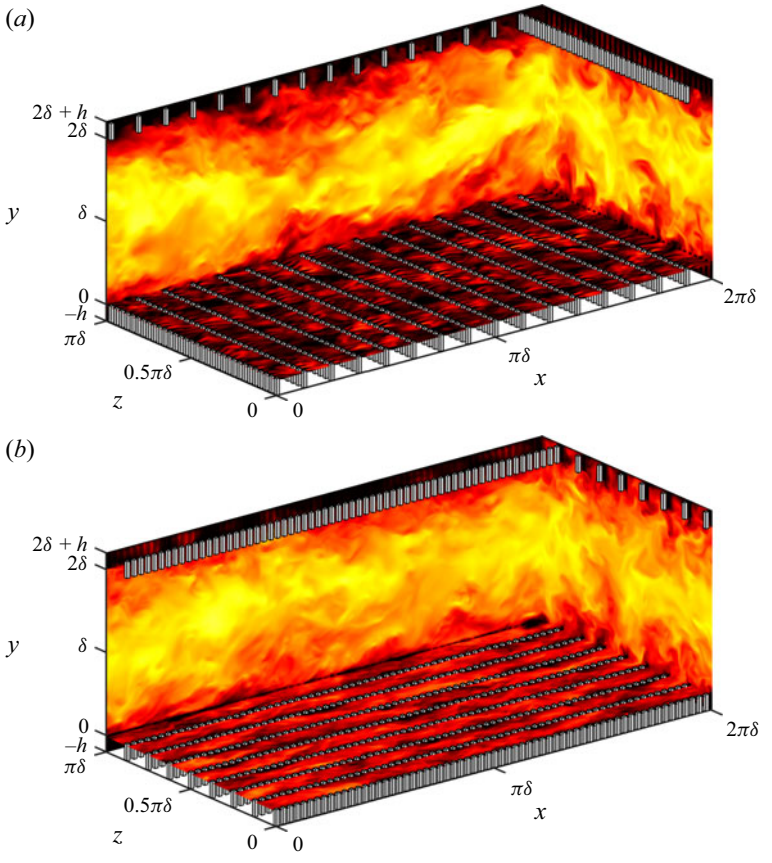


Figure 4. Schematics of the numerical channel for (*a*) spanwise-packed canopy $\mathrm{F}_{S216\times54}$, with streamwise spacing $s_x^+ \approx 216$, spanwise spacing $s_z^+ \approx 54$ and canopy height $h^+ \approx 110$, all in viscous units, and (*b*) streamwise-packed canopy $\mathrm{C}_{S54\times216}$, with $s_x^+ \approx 54$, $s_z^+ \approx 216$ and $h^+ \approx 110$. The channel half-height is δ. Details of the canopy geometries are presented in table 1. An instantaneous realisation of the streamwise velocity is shown in axis-orthogonal planes, from dark to clear $u^+ = 0$ to $u^+ = 15$ in (*a*) and $u^+ = 0$ to $u^+ = 19$ in (*b*).

$$\frac{\partial \boldsymbol{u}}{\partial t} + \boldsymbol{u}\cdot\boldsymbol{\nabla}\boldsymbol{u} = -\boldsymbol{\nabla}p + \frac{1}{Re}\nabla^2\boldsymbol{u}, \tag{2.1}$$

$$\boldsymbol{\nabla}\cdot\boldsymbol{u} = 0, \tag{2.2}$$

where $\boldsymbol{u} = \langle u, w, v\rangle$ is the velocity vector with components in the streamwise, spanwise and wall-normal directions, respectively, p is the kinematic pressure and Re denotes the bulk Reynolds number $Re = U_b\delta/\nu$ based on the bulk velocity U_b, the channel half-height δ and the kinematic viscosity ν. The simulation is operated at a constant mean pressure gradient $-\partial_x P$, with the flow rate adjusted to achieve the targeted friction Reynolds number $Re_\tau = u_\tau\delta/\nu \approx 180 - 2000$, where $u_\tau = \sqrt{\delta\,\partial_x P}$ is the reference friction velocity at the canopy-tip plane. No-slip and impermeability boundary conditions are applied at both channel walls. The rigid elements are resolved using a direct-forcing, immersed-boundary method (Mittal & Iaccarino 2005; García-Mayoral & Jiménez 2011). In this work, variables scaled with u_τ and ν are termed as in inner units, denoted by superscript $(\cdot)^+$, and those scaled with U_b and δ are referred to as in outer units.

In the wall-normal direction, a second-order central difference scheme is applied on a staggered grid. At the channel centre, where the mean shear is the weakest, the stretched

https://doi.org/10.1017/jfm.2026.11446 Published online by Cambridge University Press

wall-normal grid has a resolution $\Delta y^+_{max} \approx 3.0$ when $Re_\tau \approx 180$. At higher Reynolds numbers, where dissipation occurs at larger scales (Jiménez 2012), Δy^+_{max} extends from 3.6 to 7.0 as Re_τ increases from 360 to 2000. The finest resolution Δy^+_{min} is at the floor or canopy-tip plane, wherever the mean shear is the greatest. For all cases, $\Delta y^+_{min} \lesssim 0.3$ is satisfied when scaled with the local, dynamically relevant friction velocity, as proposed in Sharma & García-Mayoral (2018, 2020*a*).

The discretisation in the periodic, wall-parallel directions is spectral. To balance computational cost and resolution, the numerical domain is divided into blocks with different wall-parallel resolutions (García-Mayoral & Jiménez 2011). The wall blocks, containing the roughness sublayer, have a finer resolution than the block encompassing the channel centre. In the finer blocks, the grid resolution resolves not only the turbulent scales but also the canopy geometry and the element-coherent eddies, which are typically of the order of or smaller than the element width (Poggi *et al.* 2004). Consequently, the wall-parallel grid spacings in x and z are smaller than w^+_x and w^+_z. Sharma & García-Mayoral (2020*b*) examined wall-parallel resolutions for dense canopies, and concluded that a marginal resolution of 9 points per spacing and 3 points per element width for a filament canopy with $s^+ \approx 24$, $w^+ \approx 5$ and $h^+ \approx 100$ could underestimate the turbulent fluctuation within the canopy, with a maximum deviation of up to 20 % observed in the wall-normal fluctuations, although this discrepancy reduced to 4 % just above the tips. In our case, the most resolution-demanding simulations are typically those with relatively thin elements or narrow gaps, where small grid spacings are required to resolve the canopy geometry or the fluid in between elements. In table 1, the canopy with thinnest filaments is $\mathrm{G41_{S47\times47}}$, with $w^+_x = w^+_z \approx 6$ and $s^+_x = s^+_z \approx 47$, which is simulated with a resolution $\Delta x^+ = \Delta z^+ \approx 2$. For canopy $\mathrm{IS2000_{G30\times30}}$ at $Re_\tau \approx 2000$, with $w^+_x = w^+_z \approx 24$ and $s^+_x = s^+_z \approx 54$, the resolution is also marginal at $\Delta x^+ = 6$ and $\Delta z^+ \approx 3$. Such marginal resolutions are applied only for the densest canopy cases, for which fluctuations within the canopy are in any event weak compared with those above, and thus higher resolutions do not change the behaviour observed. For all other canopies, a minimum of 16 points per streamwise or spanwise pitch are used. The height of the fine blocks is chosen such that the small and rapid element-coherent eddies decay naturally before approaching the coarse block at the channel centre, which has a standard smooth-wall resolution of $\Delta x^+ \approx 8$ and $\Delta z^+ \approx 4$ (Jiménez & Moin 1991). The height above the canopy tips of the fine-resolution blocks is set to at least twice the element width for sparse canopies and twice the gap size for dense canopies, correlating with the height of the roughness sublayer (Chen & García-Mayoral 2023). This is validated *a posteriori* by examining the spectral densities of turbulent fluctuations to ensure that any small-wavelength signal has already vanished well below the inter-block interface.

2.2. *Simulation parameters*

We consider flows over canopies with rigid prismatic elements to thoroughly investigate turbulence penetration across various canopy layouts, element geometries and Reynolds numbers. We are mainly concerned with canopies fully immersed in boundary layers, so our simulations fall in the range $\delta/h = 5$-20. A few cases, in intermediate-to-dense regimes with relatively small pitch, were run at $\delta/h \approx 3.3$, but for these closely packed canopies the roughness layer scales with element spacing, rather than height (Chen & García-Mayoral 2023). Under the above conditions, an overlying turbulence, self-sustained independently of the presence of the canopy, can properly develop, and whether it penetrates within the canopy or not can be discussed. We can then expect outer layer similarity to hold. In contrast, in canopies with $\delta/h \lesssim 2$, typical of aquatic vegetation in

https://doi.org/10.1017/jfm.2026.11446 Published online by Cambridge University Press

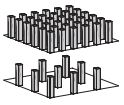
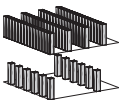
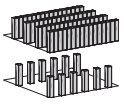
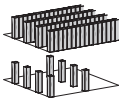
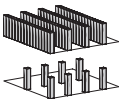
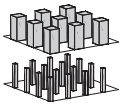
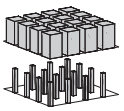
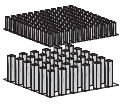
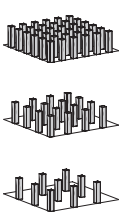
		Case	$N_x \times N_z$	Re_τ	λ_f	s_x^+	g_x^+	s_z^+	g_z^+	h^+
Isotropic		$I_{S36\times36}$	96×48	550.2	2.04	36.0	12.0	36.0	12.0	110.0
		$I_{S54\times54}$[1]	64×32	549.7	0.91	54.0	30.0	54.0	30.0	109.9
		$I_{S72\times72}$	48×24	548.2	0.51	71.8	47.8	71.8	47.8	109.6
		$I_{S108\times108}$[2]	32×16	548.7	0.23	107.7	83.8	107.7	83.8	109.7
		$I_{S144\times144}$	24×12	546.9	0.13	143.2	119.3	143.2	119.3	109.4
		$I_{S216\times216}$[3]	16×8	550.7	0.06	216.3	192.2	216.3	192.2	110.1
		$I_{S288\times288}$	12×6	551.1	0.03	288.5	264.5	288.5	264.5	110.2
		$I_{S432\times432}$	8×4	549.4	0.01	431.5	407.6	431.5	407.6	109.9
Fence		$F_{S108\times27}$[4]	32×64	548.9	0.91	107.8	83.8	26.9	3.0	109.8
		$F_{S144\times36}$	24×48	548.7	0.51	143.7	119.7	35.9	12.0	109.7
		$F_{S216\times54}$	16×32	553.4	0.23	217.3	193.2	54.3	30.2	110.7
		$F_{S288\times72}$	12×24	548.3	0.13	287.1	263.1	71.8	47.8	109.7
		$F_{S432\times108}$	8×16	548.9	0.06	431.1	407.1	107.8	83.8	109.8
Canyon		$C_{S27\times108}$[5]	128×16	552.9	0.91	27.1	3.0	108.6	84.4	110.6
		$C_{S36\times144}$	96×12	549.8	0.51	36.0	12.0	143.9	119.9	110.0
		$C_{S54\times216}$	64×8	553.6	0.23	54.3	30.2	217.4	193.2	110.7
		$C_{S72\times288}$	48×6	550.0	0.13	72.0	48.0	288.0	264.0	110.0
		$C_{S108\times432}$	32×4	548.5	0.06	107.7	83.8	430.8	406.9	109.7
Fixed s_z ($s_z^+ = 108$)		$Z_{S27\times108}$[5]	128×16	552.9	0.91	27.1	3.0	108.6	84.4	110.6
		$Z_{S108\times108}$[2]	32×16	548.7	0.23	107.7	83.8	107.7	83.8	109.7
		$Z_{S216\times108}$	16×16	548.8	0.11	215.5	191.6	107.8	83.8	109.8
Fixed s_x ($s_x^+ = 108$)		$X_{S108\times27}$[4]	32×64	548.9	0.91	107.8	83.8	26.9	3.0	109.8
		$X_{S108\times108}$[2]	32×16	548.7	0.23	107.7	83.8	107.7	83.8	109.7
		$X_{S108\times216}$	32×8	548.0	0.11	107.6	83.7	215.2	191.3	109.6
Fixed gap ($g^+ \approx 41$)		$G41_{S66\times66}$	48×24	360.7	0.63	66.1	41.3	66.1	41.3	110.2
		$G41_{S53\times53}$	48×24	359.7	0.46	53.0	41.2	53.0	41.2	109.9
		$G41_{S47\times47}$[6]	48×24	360.3	0.29	47.2	41.3	47.2	41.3	110.1
Fixed pitch ($s^+ \approx 47$)		$S47_{G14\times14}$	48×24	360.1	1.61	47.1	14.7	47.1	14.7	110.0
		$S47_{G27\times27}$	48×24	361.1	1.02	47.3	26.6	47.3	26.6	110.3
		$S47_{G35\times35}$	48×24	359.6	0.58	47.1	35.3	47.1	35.3	109.9
		$S47_{G41\times41}$[6]	48×24	360.3	0.29	47.2	41.3	47.2	41.3	110.1
Outer- similar geometry		$OS180_{G15\times15}$	48×24	179.8	0.70	23.5	14.7	23.5	14.7	44.1
		$OS360_{G30\times30}$	48×24	360.3	0.70	47.2	29.5	47.2	29.5	29.5
		$OS720_{G60\times60}$	48×24	725.5	0.70	95.0	59.4	95.0	59.4	178.0
		$OS1080_{G90\times90}$	48×24	1084.6	0.70	142.0	88.7	142.0	88.7	266.2
Inner- similar geometry		$IS550_{G30\times30}$[1]	64×32	549.7	0.91	54.0	30.0	54.0	30.0	109.9
		$IS900_{G30\times30}$	96×48	950.8	0.91	54.0	30.0	54.0	30.0	110.1
		$IS2000_{G30\times30}$	192×96	1991.9	0.91	53.8	29.9	53.8	29.9	109.6
		$IS550_{G84\times84}$[2]	32×16	548.7	0.23	107.7	83.8	107.7	83.8	109.7
		$IS900_{G84\times84}$	48×24	923.7	0.23	110.2	85.7	110.2	85.7	112.2
		$IS2000_{G84\times84}$	96×48	1974.0	0.23	111.8	87.0	111.8	87.0	113.9
		$IS550_{G192\times192}$[3]	16×8	550.7	0.06	216.3	192.2	216.3	192.2	110.1
		$IS900_{G192\times192}$	32×16	895.2	0.06	223.0	198.2	223.0	198.2	113.5
		$IS2000_{G192\times192}$	48×24	1934.2	0.06	228.8	203.4	228.8	203.4	116.4

Table 1. Simulation parameters. Here, N_x and N_z are the numbers of elements in the streamwise and spanwise directions, respectively; $Re_\tau = \delta u_\tau/\nu$ is the friction Reynolds number; λ_f is the frontal density; s_x, s_z, g_x and g_z are the pitch and gap in the streamwise and spanwise directions, respectively, and the element width is $w = s - g$; h is the canopy height. The '+' superscript indicates viscous scaling, i.e. with the friction velocity u_τ and the kinematic viscosity ν. Case names with the same superscript are the same DNS.

https://doi.org/10.1017/jfm.2026.11446 Published online by Cambridge University Press

shallow-submergence or emergent conditions, the whole flow is fully embedded within or directly affected by the canopy (Nepf & Vivoni 2000; Zhao & Nepf 2024), and an overlying turbulence cannot be meaningfully defined. The latter are therefore out of the scope of the present work.

Figure 2 illustrates the morphology of the canopies studied, and table 1 details the relevant simulation parameters. We note that in the literature, the terms 'spacing' and 'gap' are sometimes used interchangeably, mainly in the context of canopies with thin filaments, where the element width w is small compared with both s and g, so that $s = g + w \approx g$ (Cui, Patel & Lin 2003; Bailey & Stoll 2013). Here, we consider both thin filaments ($w/s \approx 0.06$) and thick and densely packed elements ($w/s \approx 0.67$). To avoid confusion, we refer to the 'spacing' s, the sum of the gap and element width, as the 'pitch' in the remainder of this work.

All canopies investigated consist of collocated prismatic elements with a square wall-parallel cross-section, with $w_x = w_z$. To distinguish among different simulations, the prefix indicates the canopy characteristics, and the subscript denotes the approximate streamwise and spanwise spacing/pitch ('S') or gap ('G') in inner units. For example, case $\mathrm{C}_{\mathrm{S27\times108}}$ refers to a canopy resembling a 'canyon' with streamwise-packed elements, where $s_x^+ \approx 27$ and $s_z^+ \approx 108$.

In table 1, the first five groups consist of canopies with identical element geometry, where $h^+ \approx 110$ and $w_x^+ = w_z^+ \approx 24$, but with different pitches and gaps. The first group, prefixed with 'I', consists of isotropic canopies with equal streamwise and spanwise pitches $s_x^+ = s_z^+$. These isotropic canopies are from Chen & García-Mayoral (2023), which showed that turbulence effectively penetrates the sparse canopy $\mathrm{I}_{\mathrm{S432\times432}}$ and perceives an origin at the floor, while turbulent eddies 'skim' over the dense canopy $\mathrm{I}_{\mathrm{S36\times36}}$ and perceives a smooth wall at the tips. The second and third groups consist of fence-like canopies prefixed with 'F', with spanwise-packed elements, and canyon-like canopies prefixed with 'C', with streamwise-packed elements, each matching the total number of posts of isotropic canopies $\mathrm{I}_{\mathrm{S54\times54}}$ to $\mathrm{I}_{\mathrm{S216\times216}}$ and therefore the value of λ_f. It will be demonstrated in § 4.1 that canopies with the same λ_f can result in different turbulence penetration behaviours, depending on whether the elements are more closely distributed in the streamwise or spanwise direction. Cheer & Koehl (1987) investigated flow through biological bristles, and showed that fence-like structures can behave as a 'paddle' (a single solid obstacle) or a 'rake' (a permeable one), depending on the gap size g^+. In the fourth group, marked by 'Z', we gradually reduce the number of posts in the streamwise direction N_x from the canyon-like canopy $\mathrm{C}_{\mathrm{S27\times108}}$, keeping all spanwise parameters (N_z, s_z^+ and g_z^+) fixed. Similarly, the fifth group, denoted by 'X', consists of canopies with different N_z but with the same streamwise parameters. In § 4.2, with the 'Z' and 'X' groups, we investigate whether parameters in the streamwise or spanwise direction have more impact on flow penetration. To identify whether the gap or pitch matters, we study canopies with a fixed gap but different pitch (group 'G') or with a fixed pitch but different gap (group 'S') in § 4.3. The number that follows prefixes 'G' and 'S' denotes the approximate value of the fixed gap and pitch in inner units, respectively. Finally, in § 4.4, we investigate the effect of the Reynolds number using canopies with similar geometry in outer (same s/δ, g/δ and h/δ in group 'OS') or inner units (same x' s^+, g^+ and h^+ in group 'IS').

3. Measuring the penetration of turbulence into the canopy

Before we embark in the analysis of canopy density, we need to establish how to measure turbulence penetration from the overlying flow. In § 3.1, we first discuss how we identify the penetrating structures that contribute to the momentum and turbulence transport in

https://doi.org/10.1017/jfm.2026.11446 Published online by Cambridge University Press

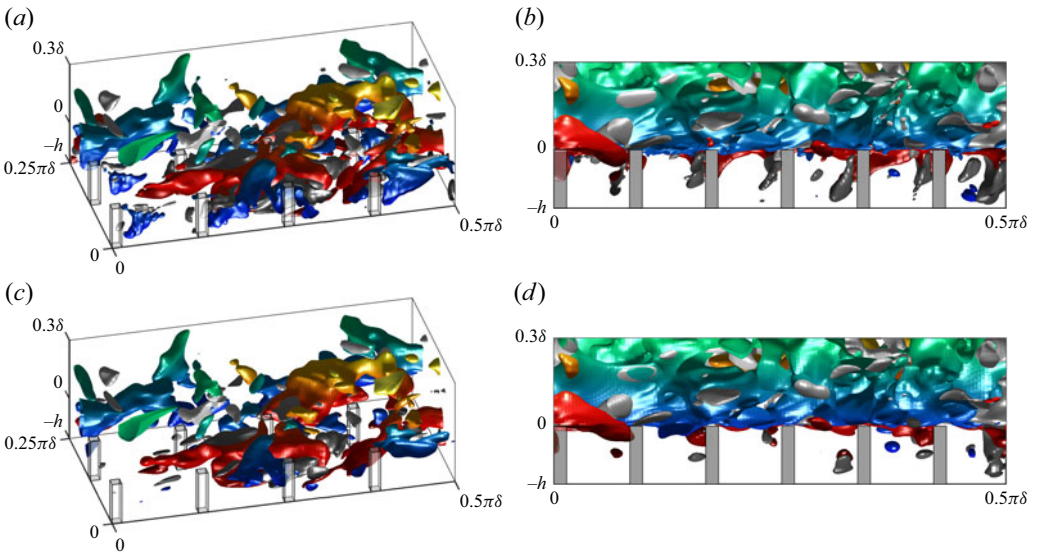


Figure 5. Instantaneous realisations of $u'v'$ structures for (a,c) case $\mathrm{I}_{S216\times216}$ and (b,d) case $\mathrm{F}_{S144\times36}$. Structures are coloured by distance to the floor, ejections in blue to green, sweeps in red to yellow and outward and inward interactions in grey to white. Panels show (a,b) raw flow fields and (c,d), flow fields spectrally filtered to remove the element-coherent flow.

the vicinity of the canopy-tip plane. In § 3.2, we introduce the metrics that we will use to quantify the penetration of these structures.

3.1. *Identification of background structures*

To investigate the penetration of the overlying background turbulence, we focus on structures of intense pointwise $u'v'$ (Lozano-Durán *et al.* 2012; Lozano-Durán & Jiménez 2014), because of their importance in momentum transport. The temporal evolution of these structures has been thoroughly studied by Lozano-Durán & Jiménez (2014); here, we are only concerned with whether they penetrate into the canopy at any given instant, and the extent of their penetration, regardless of their dynamics, and as such we do not consider their preceding or subsequent evolution.

Just like the background, turbulence can exhibit structures of intense $u'v'$, the other flow components in figure 1 can as well, including the element-coherent flow. Its structures can merge with those from the background turbulence and, if the merger is identified as a single structure, misrepresent the background turbulence as penetrating more deeply into the canopy than it actually does. To prevent this, we first filter out the element-coherent signal to isolate the background structures.

As depicted in figure 5(a), element-coherent flows typically are formed by stem-scale eddies in the wake of each obstacle. A similar pattern for stem-scale eddies is also observed in Poggi *et al.* (2004) and Sharma & García-Mayoral (2020*a*) for sparse canopies. As shown in figure 5(b), element-coherent top-shedding eddies can also form. Note that the latter are different from the canopy-scale, mixing-layer-like eddies induced by the inflectional mean profile (Raupach *et al.* 1996; Nepf 2012*a*). The element-induced, element-coherent flows shown in figure 5(a,b) are not part of the penetrating turbulence from the overlying background flow, and we therefore filter them out before measuring turbulence penetration.

https://doi.org/10.1017/jfm.2026.11446 Published online by Cambridge University Press

A conventional method to obtain the background flow is through triple decomposition (Reynolds & Hussain 1972)

$$\boldsymbol{u}(x,\,y,\,z,\,t) = \boldsymbol{U}(y) + \boldsymbol{u'}(x,\,y,\,z,\,t), \tag{3.1}$$

$$\boldsymbol{u'}(x,\,y,\,z,\,t) = \tilde{\boldsymbol{u}}(x,\,y,\,z) + \boldsymbol{u''}(x,\,y,\,z,\,t), \tag{3.2}$$

where $\boldsymbol{U}$ is the mean velocity profile, and $\boldsymbol{u'}$ is the full temporal and spatial turbulent fluctuation. The latter can be further decomposed into a time-averaged but spatially varying component, $\tilde{\boldsymbol{u}}$, and the remaining time-varying fluctuation, $\boldsymbol{u''}$. The component $\tilde{\boldsymbol{u}}$ is often referred to as the dispersive flow (Raupach & Shaw 1982) and assumed to embody the element-coherent flow. Abderrahaman-Elena, Fairhall & García-Mayoral (2019), however, suggested that the element-coherent flow is modulated in amplitude by the overlying background turbulence for roughness elements up to $h^+ \lesssim 35$.

In any event, as roughness size increases, wake unsteadiness intensifies, complicating the isolation of the background flow. For the present canopies, with sizes up to $h^+ \approx 270$ and $w^+ \approx 30$, there is significant unsteady yet element-coherent flow, rendering (3.2) ineffective as the time-dependent element-wake flow cannot be accurately represented by the temporally averaged term $\tilde{\boldsymbol{u}}$. As a practical approximation, we thus use a spectral filter to isolate the background flow, aiming to retain most of the energy of the background-turbulence wavelengths while removing the element-coherent signal. The filtering procedure is detailed in Appendix B.

The instantaneous realisations of the filtered flow field in figure 5(*c*,*d*) illustrate that both the stem-scale eddies of the sparse canopy $\mathrm{I}_{S216\times216}$ and the shedding eddies of the fence-like canopy $\mathrm{F}_{S144\times36}$ are removed effectively by the filter, while the background turbulent eddies remain essentially unmodified. The applied filter slightly reduces the volume of the largest structure in figure 5(*c*) by approximately 5 % compared with its original size in figure 5(*a*), which we deem acceptable. For case $\mathrm{F}_{S144\times36}$ in figure 5(*b*,*d*), the large structures remain essentially unaffected by the spectral filter, as they do not significantly penetrate within the 'fences' in any event. These flow visualisations suggest that the applied filtering can effectively isolate the background turbulence from the element-coherent flow.

After filtering the element-induced, element-coherent flow, we define the background structures that contribute the most to the Reynolds shear stress as connected regions satisfying

$$|u'v'(x,\,y,\,z)| > H\tau_{tip}, \tag{3.3}$$

where $u'v'(x,\,y,\,z)$ is the pointwise Reynolds shear stress, H is a thresholding constant of order ~ 1 and τ_{tip} is the total shear stress evaluated at the canopy-tip plane. The rigorous determination of a common value for H across all our simulations is discussed in Appendix C. In the discretised space of the simulations, the connectivity is established between immediately neighbouring points along x, y or z that satisfy (3.3), to ensure that only physically contiguous regions of high $|u'v'|$ are identified as a single connected structure.

3.2. *Metrics for the penetration of background-turbulence structures*

Once we have isolated the background turbulent structures from the full flow field, we can narrow our focus to the structures that cross the canopy-tip plane, as they embody turbulence penetration from above. Of the whole background, overlying turbulence, these are the eddies that come into contact with the canopy. In this subsection, we introduce measures for the location, span and volume of these 'tip-plane-intersecting' structures,

https://doi.org/10.1017/jfm.2026.11446 Published online by Cambridge University Press

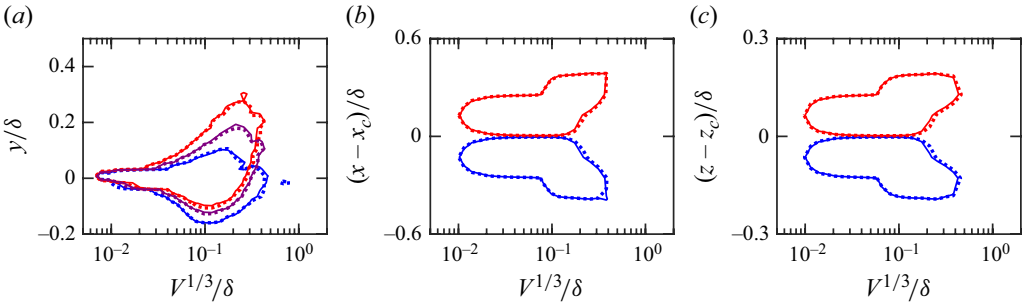


Figure 6. Probability density function (p.d.f.) of the (*a*) y, (*b*) x and (*c*) z distributions of interfacial eddies of intense $u'v'$ for canopy $\mathrm{I}_{S216\times216}$ as a function of the eddy size. Here, V is the eddy volume and δ the half-channel height. The solid and dotted contour lines represent statistics for the volume and the density of $u'v'$, respectively, and enclose 95 % of the penetrating eddies; The 25th, 50th (centroid) and 75th percentiles are represented by the red, purple and blue lines, respectively. In the wall-parallel directions, the percentile locations are measured relative to the position of the centroid, x_c-z_c.

which we will refer to as 'interfacial eddies' from here on, aiming to characterise the extent and depth of their penetration into the canopy.

The mean location of a structure can be characterised by the centroid position of its volume V

$$\boldsymbol{x}_{c,vol} = \frac{\int_{\Omega} \boldsymbol{x}(x,\,y,\,z)\mathrm{d}V}{\int_{\Omega} \mathrm{d}V}, \tag{3.4}$$

and also by the centroid position of its $u'v'$ distribution

$$\boldsymbol{x}_{c,uv} = \frac{\int_{\Omega} u'v'(x,\,y,\,z)\,\boldsymbol{x}(x,\,y,\,z)\mathrm{d}V}{\int_{\Omega} u'v'(x,\,y,\,z)\mathrm{d}V}, \tag{3.5}$$

where $\boldsymbol{x}$ is the pointwise position vector for all contiguous points within the volume of the structure, Ω. The spatial extent of a structure can be characterised by its maximum ($\boldsymbol{x}_{max}$) and minimum ($\boldsymbol{x}_{min}$) positions in x, y and z. However, we typically observe that eddies are irregular, so the absolute extrema do not necessarily provide information about where the majority of the volume and $u'v'$ are located. To quantify the spatial distribution of eddies, we instead measure the position of the nth percentile for volume ($\boldsymbol{x}_{nth,vol}$)

$$\frac{\int_{\boldsymbol{x}_{min}}^{\boldsymbol{x}_{nth,vol}} \mathrm{d}V}{\int_{\Omega} \mathrm{d}V} = \frac{n}{100}, \tag{3.6}$$

and the position of the nth percentile based on $u'v'$ intensity ($\boldsymbol{x}_{nth,uv}$)

$$\frac{\int_{\boldsymbol{x}_{min}}^{\boldsymbol{x}_{nth,uv}} u'v'(x,\,y,\,z)\mathrm{d}V}{\int_{\Omega} u'v'(x,\,y,\,z)\mathrm{d}V} = \frac{n}{100}. \tag{3.7}$$

An eddy with $y_{min} = 0.1\delta$, $y_{5th,uv} = 0.3\delta$, $y_{95th,uv} = 0.5\delta$ and $y_{max} = 0.6\delta$, for instance, would have an absolute extent in y from $y = 0.1\delta$ to $y = 0.6\delta$, but 90 % of its total $u'v'$ stress would be concentrated between $y = 0.3\delta$ and $y = 0.5\delta$, with only 5 % above and below. We denote the span of this $u'v'$-concentrated region as $y^+_{90,uv} = y^+_{95th,uv} - y^+_{5th,uv} = 0.2\delta$. As an example, figure 6 portrays the typical location of the centroid and the 25th and 75th percentiles for the penetrating eddies for a sparse canopy. Let us define a generic characteristic length scale for eddies based on their volume as $V^{1/3}$. As shown in panel (*a*), of the interfacial eddies, small ones of size $V^{1/3} \lesssim 0.03\,\delta$ tend to remain

https://doi.org/10.1017/jfm.2026.11446 Published online by Cambridge University Press

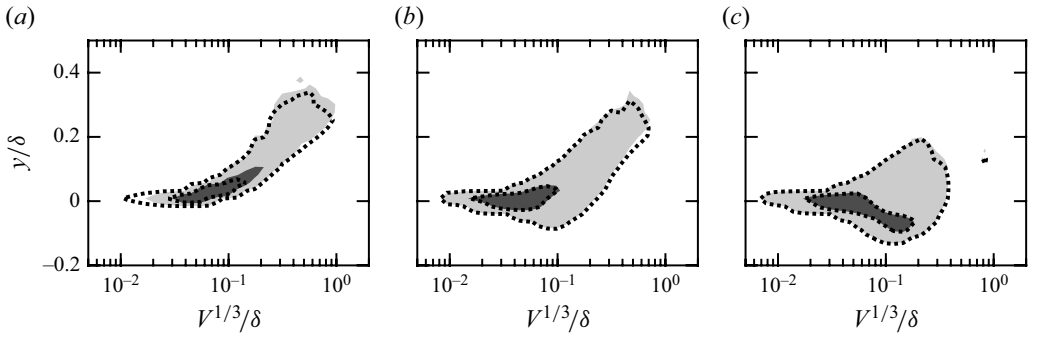


Figure 7. P.d.f. of the centroid height y for interfacial eddies of intense $u'v'$ as a function of eddy size. Here, V is the eddy volume and δ the half-channel height. Shaded contours are for the volume centroid, (3.6), and dotted ones for the $u'v'$ centroid, (3.7). Panels show (*a*) canopy $\mathrm{I}_{\mathrm{S36\times36}}$ (dense); (*b*) $\mathrm{I}_{\mathrm{S72\times72}}$ (intermediate); (*c*) $\mathrm{I}_{\mathrm{S432\times432}}$ (sparse). The contours enclose 50 % and 95 % of the eddies.

near the tips, as they cannot extend too much above or below this region due to their small size. Meanwhile, the larger eddies, of size $V^{1/3} \gtrsim 0.2\,\delta$, can effectively penetrate into the canopy, as well as extend well above the tips. Along x, panel (*b*) indicates that eddies extend relative to their centroid with upstream–downstream symmetry, with $x^+_{50,vol} \approx x^+_{50,uv} \approx 0.8\delta^+ \approx 440$; along z, panel (*c*) indicates that they also extend with left–right symmetry, with $z^+_{50,vol} \approx z^+_{50,uv} \approx 0.4\delta^+ \approx 220$. Figure 6, as well as figure 7, also shows that the eddy-size statistics based on volume and $u'v'$ are very similar, indicating that either one can be used to characterise the location and topology of the interfacial eddies. For simplicity, we present results based on volume only in the remainder of the paper, and label e.g. $z^+_{50,vol}$ simply as z^+_{50}.

The wall-normal distribution of the interfacial eddies varies significantly with canopy density, providing useful metrics to characterise the density regime. As shown in figure 7(*a*), a dense canopy like $\mathrm{I}_{\mathrm{S36\times S36}}$ precludes the overlying eddies from penetrating into it. In this case, small structures reside near the tips, while the larger ones reside essentially above the tips, with fewer than 1 % of the interfacial eddies having centroids below the tips. In contrast, a sparse canopy like $\mathrm{I}_{\mathrm{S432\times S432}}$ allows vigorous penetration of turbulent eddies into the canopy, with approximately 60 % of the interfacial eddies having centroids below the tips, as depicted in figure 7(*c*). An intermediate canopy like $\mathrm{I}_{\mathrm{S72\times S72}}$ in figure 7(*b*) lies between the two limits, with about 30 % of the interfacial eddies having centroids below the tips.

To further investigate the wall-normal distribution of eddy volume, we examine the streamwise and spanwise widths at each height of the interfacial eddies. For this, we use superficial averages at each height y in (3.6). Figure 8 illustrates the typical spanwise width of eddies z^+_{50} for dense to sparse canopies, $\mathrm{I}_{\mathrm{S36\times S36}}$, $\mathrm{I}_{\mathrm{S72\times S72}}$ and $\mathrm{I}_{\mathrm{S432\times S432}}$. For the dense canopy, panel (*a*) shows that the interfacial eddies generally have a large span compared with the element pitch, up to $z^+_{50} \approx 180$, and few of these eddies can penetrate. For the intermediate canopy, panel (*b*) shows that penetration is partially possible for eddies with widths comparable to the canopy pitch, $z^+_{50} \approx s^+_z \approx 72$, with narrower eddies with $z^+_{50} \ll s^+_z$ penetrating even deeper and reaching the floor – the influence of different canopy parameters, including s^+_z, on turbulence penetration will be further discussed in § 4. Finally, panel (*c*) shows that, for the sparse canopy, turbulence penetrates relatively unhindered, easily reaching the floor, and even deep within the canopy the characteristic eddy width remains comparable to the width at the tips. In figure 8(*a–c*), lower contour

https://doi.org/10.1017/jfm.2026.11446 Published online by Cambridge University Press

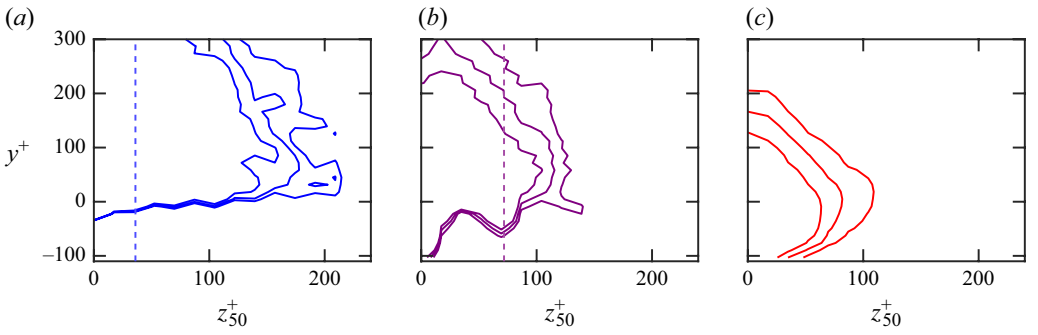


Figure 8. P.d.f. of the characteristic spanwise width z^+_{50} at each height y^+ of interfacial eddies for canopies (*a*) $\mathrm{I}_{S36\times36}$ (dense); (*b*) $\mathrm{I}_{S72\times72}$ (intermediate); and (*c*) $\mathrm{I}_{S432\times432}$ (sparse). The contours enclose 70 %, 75 % and 80 % eddies. The dashed vertical lines mark the corresponding element pitch $s^+_z \approx 36$, 72, and 432, with the latter beyond the abscissa range displayed.

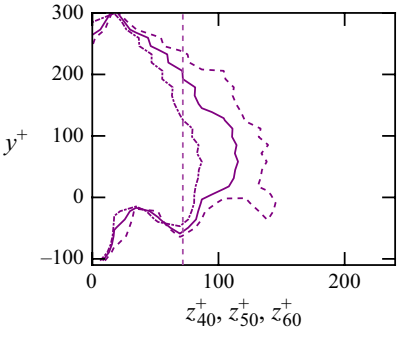


Figure 9. P.d.f. of the spanwise width at each height y^+ of interfacial eddies for canopy $\mathrm{I}_{S72\times72}$. The dash-dotted, solid and dashed contours represent widths z^+_{40}, z^+_{50} and z^+_{60}, respectively; the vertical dashed line mark the element pitch $s^+_z \approx 72$. The contours enclose 75 % of the eddies.

levels tend to capture the large-eddy tails within the probability distribution function, especially above the dense canopy and within the sparse canopy. In these regions with minimal obstruction, where the eddies are not constrained by the presence of canopy elements, turbulence spans a broader range of eddy sizes. Consequently, including a larger portion of eddies, by using a lower contour level, increases the contribution of the large but infrequent eddies. In any event, as long as the *n*th percentile captures the majority of the volume for each eddy, the characteristic width within the canopy is essentially insensitive to the choice of percentile. For illustration, figure 9 shows that spanwise widths z^+_{40}, z^+_{50} and z^+_{60} are similar within the canopy, as eddy shapes in this region are constrained by the element geometry. Only farther above the canopy, where eddies broaden and are no longer constrained, do these percentile-based widths begin to differ. For simplicity, the discussion in § 4 presents the characteristic width of eddies using x^+_{50} and z^+_{50}, with a contour level that encloses 75 % of the eddies within the p.d.f.

In addition to the typical location and size of structures, we are interested in quantifying penetration depth. We do so based on the relative planar volume V_r, defined as the fraction of the domain at each height occupied by the interfacial eddies (Del Alamo *et al.* 2006). For a sparse canopy like $\mathrm{I}_{S432\times S432}$, where turbulence can freely penetrate within, figure 10(*a*) shows that V_r decays slowly with depth into the canopy, remaining comparable to its

https://doi.org/10.1017/jfm.2026.11446 Published online by Cambridge University Press

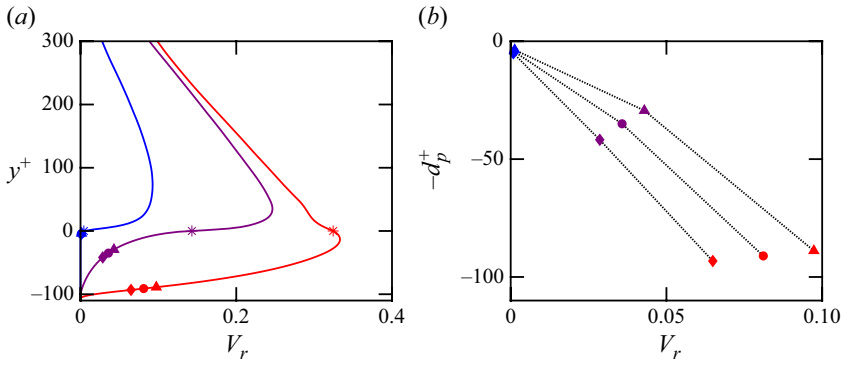


Figure 10. (*a*) Relative volume V_r occupied by interfacial eddies at each height y^+. Blue to red lines are canopies $\mathrm{I}_{S36\times36}$ (dense), $\mathrm{I}_{S72\times72}$ (intermediate) and $\mathrm{I}_{S432\times432}$ (sparse), as in figure 8. Symbols ∗, ▲, ● and ♦ indicate the height where $V_r/V_{r,tip} = 1.0$, 0.3, 0.25 and 0.2, respectively. The latter three are alternative choices for the definition of the penetration depth d_p, with $y = -d_p$, and are also portrayed in (*b*), where the dashed lines connect markers with the same value of $V_r/V_{r,tip}$ across different canopies.

footprint at the tips, $V_{r,tip}$, even deep within the canopy. For an intermediate canopy such as $\mathrm{I}_{S72\times S72}$, where turbulence penetration is partially obstructed, V_r decays more rapidly. For a dense canopy like $\mathrm{I}_{S36\times S36}$, eddies are essentially precluded from entering the canopy, and V_r vanishes immediately below the tips. Based on these observations, we define the 'penetration depth' d_p^+ as the depth below the tips at which V_r becomes small relative to its footprint at the tips. The sensitivity analysis in figure 10(*b*) demonstrates that, for $V_r/V_{r,tip} = 0.2$–0.3, d_p^+ is essentially insensitive to the chosen threshold. Dense canopies consistently result in minimal penetration, with $d_p^+ \approx 0$, while sparse canopies have penetration depths comparable to their height, $d_p^+ \approx h^+$. We thus use the threshold $V_r/V_{r,tip} = 0.25$ to determine d_p^+ from here on. This single-point indicator quantifies the depth of turbulence penetration and enables a simple comparative analysis across different canopies.

4. Results and discussion

With the metrics to quantify the extent and depth of turbulence penetration proposed above, we now apply them to our DNSs, examining the influence of one canopy parameter at a time. In § 4.1, we first explore the effect of canopy layout by making the elements closely packed in either the streamwise or spanwise direction while keeping frontal density λ_f constant. This allows us to demonstrate that the same value of λ_f does not necessarily correspond to the same density regime, as advanced in § 1. In § 4.2, we vary the pitch between elements in either the spanwise or streamwise direction to identify in which direction variations have a greater influence on turbulence penetration. In § 4.3, we vary either the element pitch or gap for isotropic canopies to determine which of the two has the most influence. In § 4.4, we investigate the same canopy at different Reynolds numbers to determine the length scale governing turbulence penetration. Finally, in § 4.5, we put together all the preceding results to propose a single parameter to encapsulate canopy density.

4.1. *Different density regimes for the same frontal density λ_f*

In this subsection, we demonstrate that frontal density λ_f alone cannot fully characterise the density for canopies with an anisotropic layout. Figure 3 illustrated that, for canopies

https://doi.org/10.1017/jfm.2026.11446 Published online by Cambridge University Press

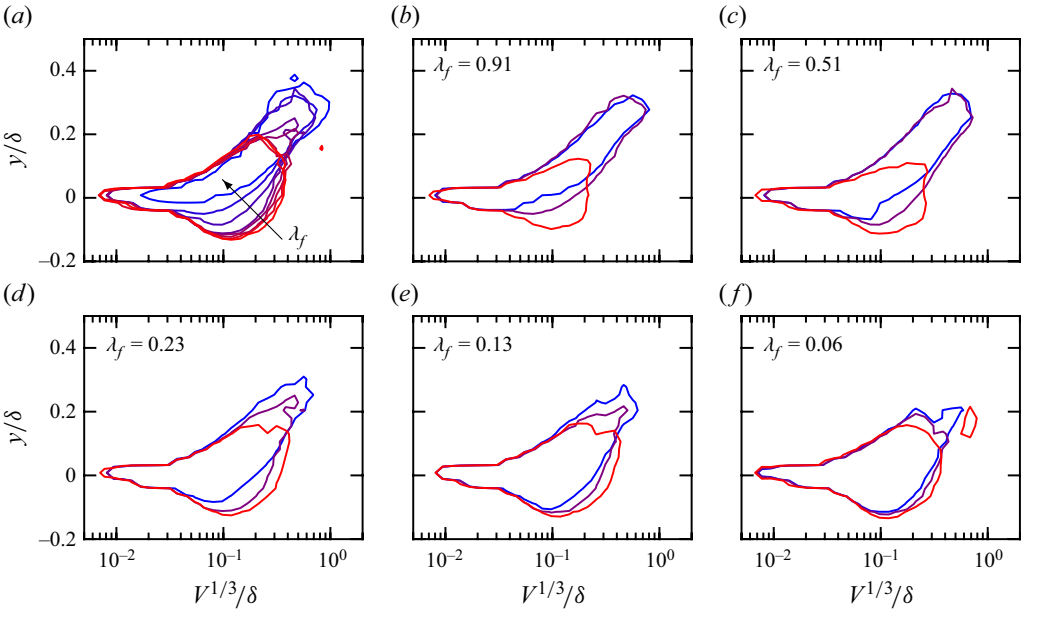


Figure 11. P.d.f. of the centroid height y of interfacial eddies as a function of eddy size. Here, V is the eddy volume and δ the half-channel height. Panels show: (*a*) isotropic-layout canopies with increasing frontal density $\lambda_f \approx 0.01$–2.04 from red to blue, increasing in the direction of the arrow; (*b–f*) decreasing frontal density $\lambda_f \approx 0.91$–0.06; blue, magenta and red indicate fence-like, isotropic and canyon-like canopies, respectively, with the same λ_f. The contours enclose 75 % of the eddies.

with the same number of elements per unit area and identical λ_f, the arrangement of elements can significantly influence how much blockage they produce on the eddies from the overlying turbulence, affecting the degree of their penetration. This difference in penetration can now be quantified with the metrics proposed in § 3.

Figure 11 depicts the typical location and size of the penetrating eddies for both isotropic and anisotropic canopies. As shown in figure 11(*a*), canopy $\mathrm{I}_{S36\times36}$, with the highest density value of $\lambda_f \approx 2.04$, behaves as dense, as less than 1 % of the eddies have centroids below the canopy-tip plane. As the elements are spaced further apart, canopies $\mathrm{I}_{S54\times54}$ and $\mathrm{I}_{S72\times72}$ allow eddies to penetrate moderately into the canopy. For these two intermediate canopies, eddies of size $V^{1/3} \gtrsim 0.05\,\delta$ can extend well above and below the tips, and more than 20 % eddies have centroids below the tips. For canopies $\mathrm{I}_{S108\times108}$ to $\mathrm{I}_{S432\times432}$, with pitch $s^+ > 100$ and $\lambda_f \approx 0.23$–0.01, turbulence penetrates with little obstruction, with more than 60 % of the eddies having centroids below the tips. Sharma & García-Mayoral (2020*a*) performed DNSs for isotropic layouts of filaments, and argued that canopies were sparse if the pitch between elements was $s^+ > 100$, which allowed sufficient space for near-wall streaks to fit within. However, while λ_f captures the overall trends of turbulence penetration in dense and intermediate canopies, it fails to distinguish the sparser canopies $\mathrm{I}_{S108\times108}$ to $\mathrm{I}_{S432\times432}$ in figure 11(*a*), which essentially have similar distributions of centroids. More importantly, figure 11(*b–f*) illustrates that the same value of λ_f does not necessarily result in the same density regime. For instance, canopies with $\lambda_f \approx 0.91$ would typically be classified as dense based on λ_f alone (Nepf 2012*a*; Brunet 2020). However, as shown in figure 11(*b*), although the isotropic and the fence-like canopies $\mathrm{I}_{S54\times54}$ and $\mathrm{F}_{S108\times27}$ behave as dense, the canyon-like canopy $\mathrm{C}_{S27\times108}$, with the same λ_f, behaves as sparse, with approximately 65 % of the interfacial eddies having centroids below the

https://doi.org/10.1017/jfm.2026.11446 Published online by Cambridge University Press

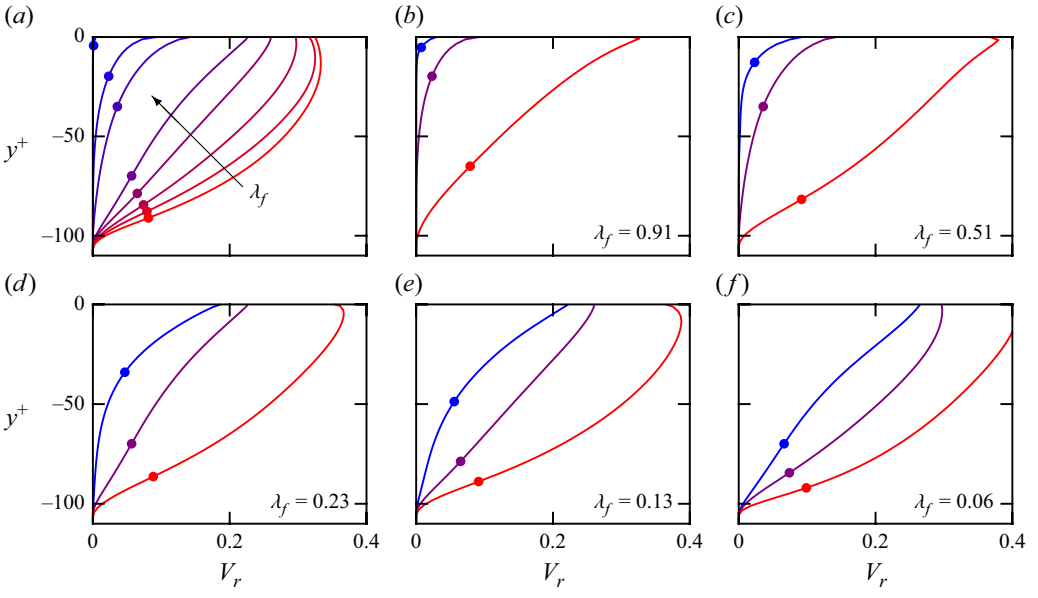


Figure 12. Relative volume V_r occupied by interfacial eddies at each height y^+. Markers • indicate the penetration depth $y^+ = -d_p^+$ where $V_r/V_{r,tip} = 0.25$. The canopies portrayed in each panel and the colour scheme are the same as in the respective panels in figure 11: (*a*) isotropic-layout canopies with increasing frontal density $\lambda_f \approx 0.01$–2.04 from red to blue, increasing in the direction of the arrow; (*b*) through (*f*) decreasing frontal density $\lambda_f \approx 0.91$–0.06; blue, magenta and red indicate fence-like, isotropic and canyon-like canopies, respectively, with the same λ_f.

tips. At lower densities, the isotropic and fence-like canopies allow eddies to penetrate more effectively, see figure 11(*c–e*) , while canyon-like canopies consistently result in the most significant turbulent penetration for a given λ_f. Eventually, for low enough frontal densities $\lambda_f \lesssim 0.06$, turbulence can enter freely into the canopies regardless of the canyon, fence or isotropic layout.

In addition to examining the distribution of centroids, we also analyse the penetration depth d_p^+ of eddies below the canopy-tip plane, as portrayed in figure 12. In agreement with figure 11(*a*), figure 12(*a*) illustrates that turbulence only penetrates moderately into the dense to intermediate canopies $\mathrm{I}_{S36\times36}$ to $\mathrm{I}_{S72\times72}$, with $d_p^+ \gtrsim 35$. In contrast, turbulence penetrates significantly deeper into the sparser canopies $\mathrm{I}_{S108\times108}$ to $\mathrm{I}_{S432\times432}$, where $d_p^+ \approx 70$–91. Figure 12(*b–f*) shows that the influence of element layout is more noticeable for canopies with a higher value of frontal density $\lambda_f \gtrsim 0.51$, where the isotropic and the fence-like layouts induce more blockage on the overlying eddies compared with the canyon-like layout. However, once the frontal density is small, $\lambda_f \lesssim 0.06$, the canopy behaves as sparse regardless of its layout anisotropy, suggesting that λ_f provides only a notional measure of density for denser canopies. As depicted in figure 12(*b*,*c*), the isotropic and the fence-like canopies essentially preclude the eddies from entering the canopy, whereas the canyon-like canopy allows effective turbulence penetration, with $d_p^+ \approx 65$ even at $\lambda_f \approx 0.91$. As λ_f decreases, the isotropic and the fence-like canopies in figure 12(*d*,*e*) allow turbulence to penetrate within, but they consistently behave as denser compared with the corresponding canyon-like canopies. In the sparse limit, $\lambda_f \lesssim 0.06$, turbulence penetrates freely into the canopy, regardless of the layout. We also note that the canyon-like canopies in figure 12(*b–f*) appear as sparse for all λ_f considered, with $d_p^+ \gtrsim 65$–92. The observations in figures 11 and 12 suggest that the depth of turbulence

https://doi.org/10.1017/jfm.2026.11446 Published online by Cambridge University Press

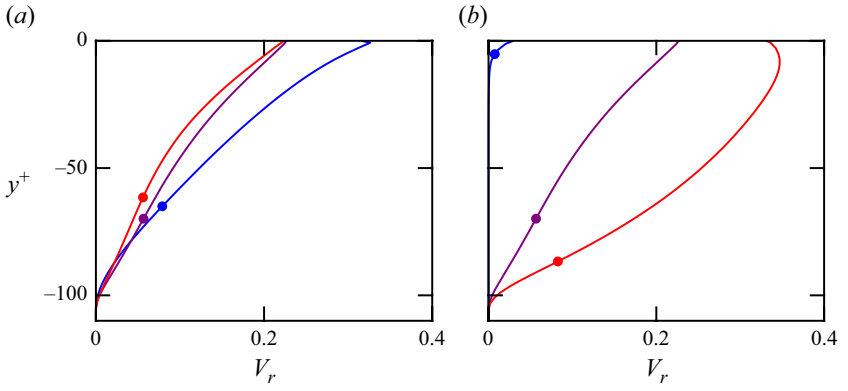


Figure 13. Relative volume V_r occupied at each height y^+ by interfacial eddies: canopies with (*a*) fixed $s_z^+ \approx 108$ and (*b*) fixed $s_x^+ \approx 108$. Blue, purple and red lines are for canopies with frontal densities $\lambda_f \approx 0.91$, 0.23 and 0.11, respectively. Markers • indicate the penetration depth $y^+ = -d_p^+$ where $V_r / V_{r,tip} = 0.25$.

penetration has a dependence on whether the canopy elements are closely packed in the streamwise or spanwise direction, with the former behaving as sparser. In §§ 4.2 and 4.3, we will further examine the effects of element pitch and gap in different directions.

4.2. *Influence of streamwise and spanwise pitch*

We have shown that, for a fixed λ_f, the location of interfacial eddies and their penetration depth depend on whether the canopy elements are more closely packed in the streamwise or spanwise direction. To further investigate the effect of the streamwise and spanwise arrangement, we now vary the element pitch, i.e. spacing, separately in the streamwise and spanwise directions while keeping the element geometry fixed. This allows us to examine the effect of s_x^+ and s_z^+ independently, and to better understand how canopy anisotropy affects turbulence penetration. We thus focus on the results for canopies $\mathrm{Z}_{\mathrm{S27\times108}}$, $\mathrm{Z}_{\mathrm{S108\times108}}$ and $\mathrm{Z}_{\mathrm{S216\times108}}$ on one hand, and $\mathrm{X}_{\mathrm{S108\times27}}$, $\mathrm{X}_{\mathrm{S108\times108}}$ and $\mathrm{X}_{\mathrm{S108\times216}}$ on the other.

Detailed, quadrant-wise results for the penetration of $u'v'$ eddies for these canopies are presented and discussed in Appendix D. The canopies with a fixed spanwise pitch, $s_z^+ \approx 100$, allow turbulence to penetrate effectively within, with no significant influence of the value of s_x^+. In contrast, canopies with a fixed streamwise pitch, $s_x^+ \approx 100$, exhibit different penetration behaviours depending on their spanwise pitch. The canopy with $s_z^+ \approx 25$ significantly restricts turbulence penetration, while the canopies with $s_z^+ \approx 100$ and $s_z^+ \approx 200$ increasingly allow turbulence to penetrate. This is also shown in figure 13(*a*), which portrays eddy volume reduction and penetration depth into the canopy for the above cases. All the canopies with common spanwise pitch $s_z^+ \approx 100$ behave as sparse, regardless of their frontal density $\lambda_f \approx 0.11$–0.91 and streamwise pitch $s_x^+ \approx 25$–200, allowing eddies to effectively penetrate into the canopy with a penetration depth $d_p^+ \approx 65$, as portrayed in figure 13(*a*). In contrast, figure 13(*b*) highlights that when the pitch in x is fixed to $s_x^+ \approx 108$, the canopies behave as increasingly sparser as the spanwise pitch increases from $s_z^+ \approx 25$ to $s_z^+ \approx 200$. This transition in density regime is marked by a substantial increase in penetration depth, from $d_p^+ \approx 5$ for the dense canopy $\mathrm{X}_{\mathrm{S108\times27}}$ to $d_p^+ \approx 87$ for the sparse canopy $\mathrm{X}_{\mathrm{S108\times216}}$.

https://doi.org/10.1017/jfm.2026.11446 Published online by Cambridge University Press

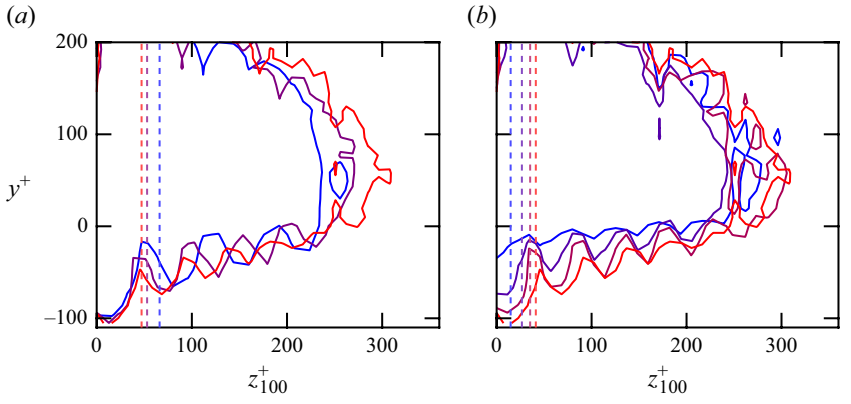


Figure 14. P.d.f. of the total spanwise width of interfacial eddies, $z^+_{100} = z^+_{max} - z^+_{min}$, at each height y^+ for canopies with (*a*) fixed gap $g^+_z \approx 41$ and (*b*) fixed pitch $s^+_z \approx 47$. The contours from blue to red represent canopies with decreasing frontal densities, $\lambda_f \approx 0.63, 0.46, 0.29$ in (*a*), and $\lambda_f \approx 1.61, 1.02, 0.58, 0.29$ in (*b*); the dashed lines mark the corresponding pitch $s^+_z \approx 66, 53, 47$ in (*a*) and gap $g^+_z \approx 15, 27, 35, 41$ in (*b*). The contours enclose 75 % of the interfacial eddies.

The correlation between turbulence penetration and spanwise pitch is not surprising; as turbulence is advected downstream, eddies will be obstructed by the elements they encounter. In turn, when the elements are spaced further apart in the spanwise direction, once eddies have penetrated within the canopy they will travel through the canyons without encountering any significant obstruction. We note that this argument is based on turbulent eddies being advected downstream, essentially travelling with the local mean flow, rather than on their length or length-to-span aspect ratio. Eddies penetrating significantly within the canopy need pathways through which they can travel relatively unhindered, rather than gaps where they can fit, as if motionlessly, in between canopy elements.

4.3. *Influence of element pitch versus gap width*

We have shown that, as the canopy elements are spaced further apart in the spanwise direction, the canopy transitions to a sparser regime, whereas variations in the streamwise direction have little impact on the density regime. However, it remains to be determined whether this difference in turbulence penetration is due to the increase in gap, g^+_z, or in pitch i.e. spacing, s^+_z. We address this question by examining canopies with either a fixed inter-element gap and varying element pitch or a fixed pitch and varying gap.

To illustrate how s^+_z and g^+_z influence the 'accessible space' that penetrating eddies must fit within, figure 14 depicts the total spanwise width of interfacial eddies z^+_{100} at each height; further, quadrant-wise results are presented and discussed in Appendix D. As shown in panel (*a*), within the canopies with a fixed gap $g^+_z \approx 41$, the distribution of z^+_{100} remains largely similar, regardless of the variations in s^+_z. In contrast, panel (*b*) shows that increasing g^+_z while keeping s^+_z constant enables eddies with larger widths to penetrate more easily into the canopy, suggesting that gap width, rather than pitch, determines the 'accessibility' of the canopy for turbulence penetration. For all canopies considered in figure 14, only eddies with widths smaller than the gap size, $z^+_{100} < g^+_z$, can penetrate all the way into the canopy. When this gap is very small ($g^+_z \lesssim 15$), not even the smallest turbulent structures, of size $\lambda^+ \sim \mathcal{O}(20)$ (Jiménez 2012; Jiménez 2013), can fit in between the elements, and thus turbulence penetration is essentially fully impeded, as evidenced by the results for canopy $\mathrm{S47_{G14\times14}}$ in figure 14(*b*). We note that eddies with a span between

https://doi.org/10.1017/jfm.2026.11446 Published online by Cambridge University Press

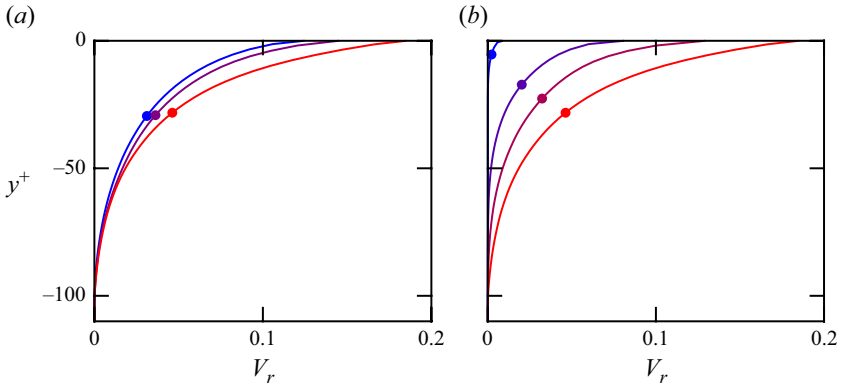


Figure 15. Relative volume V_r occupied at each height y^+ by interfacial eddies. Canopies with (*a*) fixed gap $g_z^+ \approx 41$ and (*b*) fixed pitch $s_z^+ \approx 47$. Markers • indicate the penetration depth $y^+ = -d_p^+$ where $V_r/V_{r,tip} = 0.25$. The colour scheme is as in figure 14: from blue to red, canopies with decreasing frontal densities; (*a*) $\lambda_f \approx 0.63, 0.46, 0.29$ and (*b*) $\lambda_f \approx 1.61, 1.02, 0.58, 0.29$.

g_z and s_z, which would directly conflict with the canopy elements of width $w_z = s_z - g_z$, are in particular less likely to penetrate as deep as those slightly smaller and, to a lesser extent, those slight larger, which would still need to circumvent obstructing elements. This gives the contours of the p.d.f. their characteristic serrated shape.

In agreement with figure 14, figure 15 portrays the dependence of the penetration depth on the spanwise gap between elements. As shown in figure 15(*a*), the penetration depth remains similar for cases with fixed gap size, $d_p^+ \approx 30$, independently of variations in pitch. However, figure 15(*b*) demonstrates that canopies behave as sparser with increasing spanwise gap g_z^+. As the spanwise gap widens from $g_z^+ \approx 15$ to $g_z^+ \approx 40$, the penetration depth increases from $d_p^+ \approx 5$ to $d_p^+ \approx 30$. The main contribution to the net eddy volume within the canopies is from fourth-quadrant sweep structures, which typically have a larger width within the canopy compared with those from the other quadrants, as demonstrated in figure 32(*d*,*h*) in Appendix D.

4.4. *Influence of the Reynolds number*

We have so far argued that the penetration of the overlying turbulence depends on whether the span of canopy 'canyons' is sufficient for the interfacial turbulent eddies to fit within. This inherently involves not only the canopy dimensions, but also the characteristic dimensions of those eddies. Assuming that their dimensions are set by the overlying turbulent dynamics, classical scaling would imply that they scale in inner units if they are sufficiently embedded in the near-wall region, and with the height above a notional wall if they lie farther above and into the log layer. The governing parameter would be the zero-plane-displacement depth below the plane of tips, d_0^+, the depth perceived as the origin by the overlying-turbulence eddies, which we have recently reported in detail for a wide range of canopy densities (Chen & García-Mayoral 2023). For most of the present cases, with low to moderate Reynolds numbers and $d_0^+ \lesssim 100$, we would expect interfacial eddies to scale in inner units. To investigate this, we examine canopies with either the same dimensions in inner units (same s^+, g^+ and h^+) or in outer units (same s/δ, g/δ and h/δ), for different frontal densities λ_f and across different Reynolds numbers Re_τ.

Figure 16 depicts the decay rate of the eddy volume and the penetration depth for both the 'inner-similar' and the 'outer-similar' canopies from table 1. As shown in panels (*a–c*) and (*e–g*), when a canopy remains the same in inner units for varying Re_τ, be it

https://doi.org/10.1017/jfm.2026.11446 Published online by Cambridge University Press

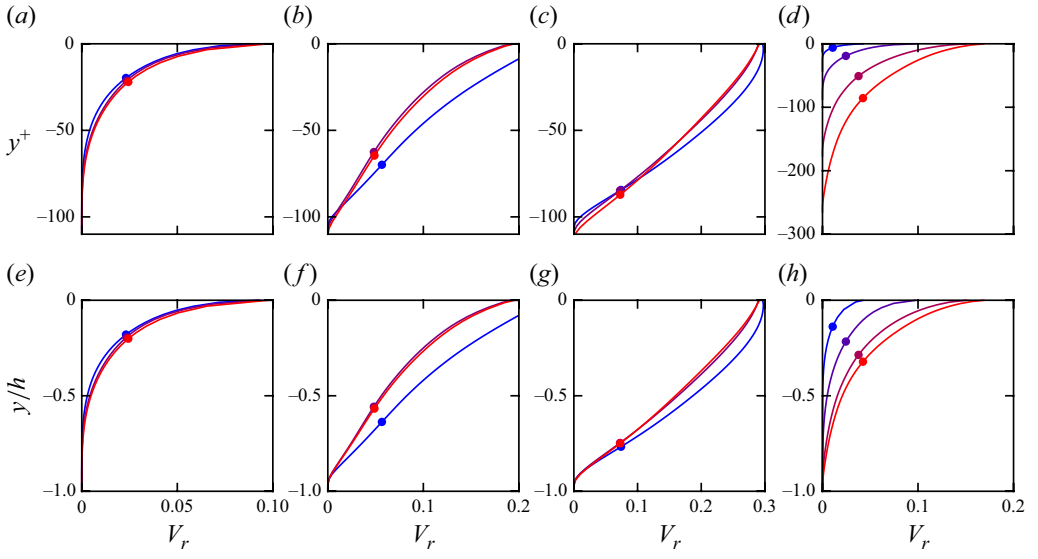


Figure 16. Relative volume V_r occupied at each height y^+ by interfacial eddies. Panels (a,e), (b,f) and (c,g) are respectively for $\lambda_f \approx 0.91$, 0.23 and 0.06, 'inner-similar' canopies with the same s^+, g^+ and h^+; (d,h) are 'outer-similar' canopies with $\lambda_f \approx 0.70$ and the same s/δ, g/δ and h/δ. Lines from blue to red indicate increasing Reynolds number $Re_\tau \approx 550$–2000. Markers • indicate the penetration depth $y = -d_p$ where $V_r/V_{r,tip} = 0.25$.

dense as in panels (a,e), intermediate as in (b,f) or sparse as in (c,g), it exhibits similar turbulent penetration. This is consistent with the scaling of interfacial eddies in viscous units mentioned above. Scaling of the flow in inner units over canopies and rough surfaces has also been reported by Chan *et al.* (2015) and Sharma & García-Mayoral (2020*a*,*b*) at Re_τ and s^+-h^+ values comparable to the present ones.

In contrast, a canopy that remains the same in outer units, i.e. with fixed s/h and g/h but varying g^+ and all other dimensions in viscous units, can exhibit different behaviours as Re_τ varies. This is portrayed for the canopy of $\mathrm{OS180_{G15\times15}}$ in figure 16(d,h). This canopy behaves as dense at $Re_\tau \approx 180$, for which $d_p^+ \approx 5$ and the turbulence essentially skims above, with limited penetration. However, for increasing Reynolds numbers, the canopy behaves as increasingly sparser, as the penetration depth increases gradually to $d_p^+ \approx 85$ at $Re_\tau \approx 1080$, for which d_p^+ is of the order of the zero-plane displacement d_0^+. The increase in d_p^+ is not linear with the canopy dimensions in inner units, e.g. with g_z^+, which would result in a collapse of the results in figure 16(h). For $g_z^+ \approx 15$, eddy penetration is negligible, and only for $g_z^+ \gtrsim 30$ does it begin to approach $d_p \approx g_z$, with an eventual collapse in panel (h). This is what one would expect if the impedance exerted by the canopy elements on the interfacial eddies was essentially viscous for $g_z^+ \approx 15$, but became increasingly inertial for $d_0^+ \approx 50$–100; interfacial eddies would then scale with d_0, and the vanishing effect of viscosity would result in $d_0 \sim d_p \sim g_z$. Finally, we note that the increase in penetration depth has been observed for a canopy with $d_p \approx 0.15\,h - 0.35\,h$, and would not occur for a sparse canopy with $d_p \approx h$, for which no further increase of d_p would be possible due to the presence of the flow. The conclusion is that canopies that are sparse at low Re_τ remain sparse as Re_τ increases, while dense ones can behave as increasingly sparse as the interfacial eddy size decreases relative to the canopy gap. We expect, however, that this effect eventually saturates, as the penetration depth asymptotes

https://doi.org/10.1017/jfm.2026.11446 Published online by Cambridge University Press

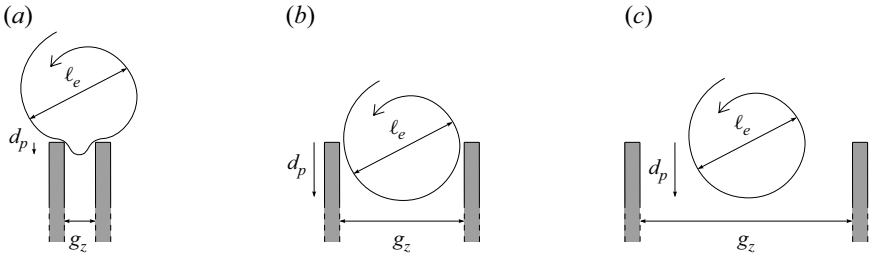


Figure 17. Sketch of the penetration depth d_p for interfacial eddies of size ℓ_e, depending on the value of ℓ_e relative to the spanwise gap between canopy elements, g_z: (*a*), $\ell_e > g_z$; (*b*), $\ell_e \sim g_z$; (*c*), $\ell_e < g_z$.

to $d_p \approx g_z$; verifying this will require measurements at Reynolds numbers higher than our current computational capability.

4.5. *What makes a canopy dense or sparse?*

The preceding discussion suggests that, depending on the ratio between canopy gap g_z and the width of interfacial eddies ℓ_e, the eddies will be in one of the situations sketched in figure 17. For closely packed elements, $g_z < \ell_e$, the eddies would not fit in the gaps, and their penetration would be limited, as sketched in panel (*a*), to a few viscous units if $g_z^+ \lesssim 15$ or to order $d_p \sim g_z$ otherwise. For a wider separation between elements, such that $g_z \sim \ell_e$ as in panel (*b*), eddies could penetrate into the canopy, but the depth of the penetration would be limited by their own size, as the span-to-height ratio of wall turbulent eddies is of order unity (Flores & Jiménez 2010). We would then have $d_p \sim g_z$ once more. For widely separated elements, $g_z > \ell_e$ as in panel (*c*), interfacial eddies could traverse the plane of the tips freely and penetrate into the canopy undisturbed, but the penetration depth would again be limited by the eddy size itself, yielding $d_p \sim \ell_e < g_z$. The latter case is only possible if the zero-plane displacement d_0, which sets the scale for the eddy size ℓ_e, is small enough to result in $\ell_e < g_z$. This in turn is only possible if d_0 is restricted by the proximity of the floor, rather than by g_z, that is, for sparse canopies with $d_p \approx h$.

Given the limited Re_τ in our simulations, let us first assume that across our canopies the interfacial eddy size broadly scales in viscous units. If that is the case, g_z^+ would be a reasonable surrogate for the ratio g_z/ℓ_e, and can therefore be used to characterise eddy penetration. This is illustrated in figure 18, which shows that g_z^+ is a good predictor for d_p^+ and significantly outperforms the classic frontal density λ_f. Starting at small g_z^+, the penetration depth d_p^+ increases monotonically with g_z^+ until it eventually becomes comparable to the canopy height, which is $h^+ \approx 100$ for most of our canopies. The only exception are the 'outer-similar' canopies discussed in § 4.4, which have $h^+ \approx 50$–270 and for which the last case has $d_p^+ \approx 85$, still far from the full canopy height $h^+ \approx 270$. This case appears as a slight outlier in figure 18(*a*).

The question that arises then is if, for our sparse canopies with eddy penetration essentially all the way to the floor, that penetration is restricted by the presence of the floor, or if is it is already as much as it would be if the floor were further below. To address this, we have run three additional simulations for a dense, an intermediate and a sparse canopy in which we doubled the canopy height. The parameters of the simulations are summarised in table 2, which also includes the original simulations for reference. The results for d_p^+ are shown in figure 19(*a*). For dense and intermediate canopies, doubling the canopy height from $h^+ \approx 110$ to $h^+ \approx 220$ results in no significant change in the penetration depth d_p^+, which remains essentially $d_p \approx g_z$. This is consistent with the representations for eddy

https://doi.org/10.1017/jfm.2026.11446 Published online by Cambridge University Press

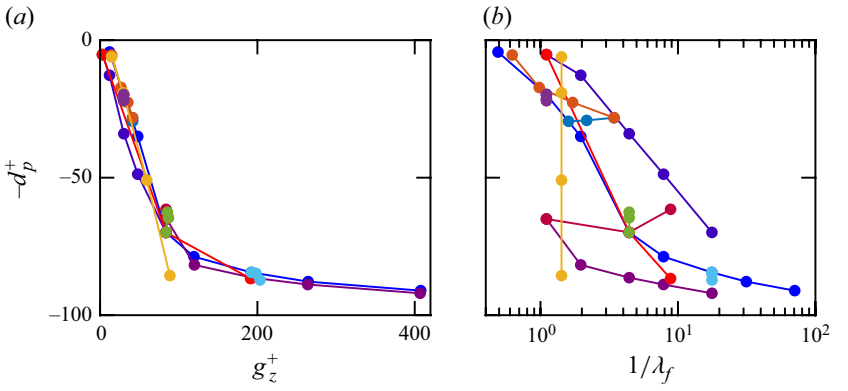


Figure 18. Penetration depth d_p^+ versus (a) spanwise gap g_z^+ and (b) frontal density λ_f. ●, isotropic-layout canopies; ●, 'fence-like' canopies; ●, 'canyon-like' canopies; ●, fixed-s_z canopies; ●, fixed-s_x canopies; ●, fixed-gap canopies; ●, fixed-pitch canopies; ●, 'outer-similar' canopies; ●, 'inner-similar' canopies with $\lambda_f \approx 0.91$; ● 'inner-similar' canopies with $\lambda_f \approx 0.23$; ● 'inner-similar' canopies with $\lambda_f \approx 0.11$. The coloured lines connect cases in the corresponding set.

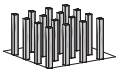
		Case	$N_x \times N_z$	Re_τ	λ_f	g_z^+	g_x^+	s_z^+	s_x^+	h^+
Different height		$I_{S54\times54}$	64×32	549.7	0.91	30.0	30.0	54.0	54.0	109.9
		$I_{S108\times108}$	32×16	548.7	0.23	83.8	83.8	107.7	107.7	109.7
		$I_{S216\times216}$	16×8	550.7	0.06	192.2	192.2	216.3	216.3	110.1
		$H220_{S54\times54}$	64×32	549.2	1.81	30.0	30.0	53.9	53.9	219.7
		$H220_{S108\times108}$	32×16	550.9	0.45	84.1	84.1	108.2	108.2	220.4
		$H220_{S216\times216}$	16×8	551.6	0.11	192.6	192.6	216.6	216.6	220.7

Table 2. Simulation parameters for canopies with height doubled to $h^+ \approx 220$. The corresponding simulations with $h^+ \approx 110$ from table 1 are also included for reference.

penetration in figure 17(a–b). For the sparse canopy, however, doubling the canopy height results in an increase in d_p^+, and an approach to the $d_p \approx g_z$ trend of denser canopies. This would correspond to a transition from the representation of figure 17(c) to the one in figure 17(b), and illustrates a secondary role of canopy height in the penetration of the overlying turbulence. We have so far considered the penetration of interfacial eddies as driven essentially by the dynamics and canopy properties at the interface with the overlying flow. For sparse canopies with $d_p \approx h$, however, increasing their height can have the direct result of increasing the depth of the zero-plane displacement. This, in turn, results in an increase of the typical size of interfacial eddies, and thus of their penetration depth, $d_p \sim \ell_e$, which can continue until they reach $\ell_e \approx g_z$, when the penetration depth begins to be limited by the canopy canyon width.

Ultimately, canopy density can be characterised by what proportion of the canopy the overlying turbulence can penetrate, that is, by d_p/h. From the above discussion, we expect d_p/h to be roughly proportional to g_z/h for dense and intermediate canopies, and to approach $d_p/h \approx 1$ for sparse ones. This suggests that density can be characterised in a graph of d_p/h vs. g_z/h, as portrayed in figure 19(b). The figure is similar to figure 18(a), but the largest 'outer-similar' case, as well as the simulations with doubled height of figure 19(a), no longer appear as outliers, and collapse with the rest. The figure shows

https://doi.org/10.1017/jfm.2026.11446 Published online by Cambridge University Press

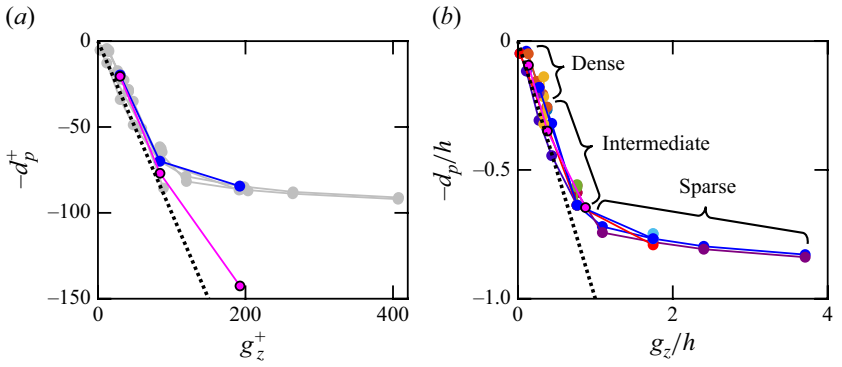


Figure 19. Penetration depth versus spanwise gap, scaled (*a*) in viscous units as in figure 18(*a*), and (*b*) with the canopy height h. • and •, cases 'I' and 'H220' from table 2, respectively. In (*a*), • is used for cases already portrayed in figure 18. In (*b*), colours are as in figure 18. The coloured lines connect cases in the corresponding set. The dotted lines are $d_p = g_z$.

that canopies lie along the line $d_p/h = g_z/h$ for $g_z/h \lesssim 0.5$, and tend to a constant $d_p/h \approx 0.9$ for $g_z/h \gtrsim 1$. In any event, if we characterise density in terms of what proportion of the canopy the overlying turbulence can penetrate, dense canopies would be those with small penetration depth relative to the canopy height, e.g. $d_p/h \lesssim 0.2$, sparse ones those with substantial penetration, e.g. $d_p/h \gtrsim 0.7$, and those in between would have intermediate density and connect the two aforementioned limit trends. From the inspection of figure 19(*b*), intermediate canopies mostly lie along the $d_p \approx g_z$ trend of dense ones; the difference between the two is not in their trend in the figure, but merely in percentage of the canopy accessible to the overlying turbulence. Expressed in terms of gap-to-height ratio, dense canopies would then have $g_z/h \lesssim 0.2$, intermediate ones $0.2 \lesssim g_z/h \lesssim 1$ and sparse ones $g_z/h \gtrsim 1$.

4.6. *Beyond collocated layouts*

The present work has focused solely on canopies of collocated, i.e. streamwise- and spanwise-aligned, elements. In this case, the concept of a spanwise gap as a 'canyon width' through which turbulent eddies can travel unobstructed is straightforward to define. While the concept of a canyon width determining the extent of eddy penetration should apply to other element layouts, quantifying this may be less straightforward and is left for future work. As a first, preliminary, step to how this would play out, let us consider staggered layouts. For this, we have run a few additional simulations, listed in table 3, where we have taken some of our original isotropic canopies, also listed for reference, with spanwise gaps $g_z^+ \approx 30$, 50, 85 and 120, and shifted consecutive rows of elements by half a period either in x (canopies SX) or in z (canopies SZ), as indicated in the sketches in the table.

In terms of 'canyon width', we would expect the staggering in x not to have an effect on the effective g_z. In turn, for elements staggered in z, we would in principle assume the effective gap to be the one when viewing the 'canyons' from the front, $g_z'^+$. This frontal gap, however, can quickly become vanishingly small, even when there is still significant room for the flow to travel in between elements, as sketched in figure 20. Intuitively, we would then expect that the effective gap was larger than the frontal one.

Figure 21 portrays eddy penetration for x- and z-staggered canopies vs. g_z and g_z'. For x-staggered canopies, the results suggest that there is indeed no effective change in gap with respect to collocated ones. For z-staggered canopies, the results suggest that the effective gap width is smaller than g_z, but larger than $g_z'^+$. There is always some degree

https://doi.org/10.1017/jfm.2026.11446 Published online by Cambridge University Press

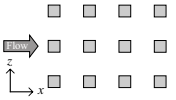
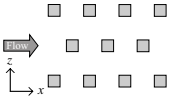
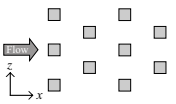
		Case	λ_f	s_z^+	g_z^+	$g_z'^+$	$\widehat{g}_z^+$
Isotropic		$\mathrm{I}_{S54\times54}$	0.91	54.0	30.0	54.0	30.0
		$\mathrm{I}_{S72\times72}$	0.51	71.8	47.8	71.8	47.8
		$\mathrm{I}_{S108\times108}$	0.23	107.7	83.8	107.7	83.8
		$\mathrm{I}_{S144\times144}$	0.13	143.2	119.3	143.2	119.3
Staggered in X		$\mathrm{SX}_{S27\times54}$	0.91	54.1	30.1	30.1	16.1
		$\mathrm{SX}_{S36\times72}$	0.51	72.1	48.0	48.0	32.2
		$\mathrm{SX}_{S54\times108}$	0.23	108.1	84.1	84.1	64.4
Staggered in Z		$\mathrm{SZ}_{S54\times27}$	0.91	53.9	29.9	3.0	16.1
		$\mathrm{SZ}_{S72\times36}$	0.51	72.0	48.0	12.0	32.2
		$\mathrm{SZ}_{S108\times54}$	0.23	108.2	84.2	30.1	64.4
		$\mathrm{SZ}_{S144\times72}$	0.13	143.5	119.6	47.8	96.3

Table 3. Simulation parameters for canopies with staggered layouts. The corresponding isotropic canopies from table 1 are also included for reference. The staggered arrangements are offset by half a canopy pitch in either the streamwise (x) or spanwise (z) direction, as illustrated in the top-view sketches. The pitch s^+ and the gap g^+ are defined based on the values for the corresponding isotropic configuration, and the frontal and effective gaps, $g_z'^+$ and $\widehat{g}_z^+$, are defined according to figure 20.

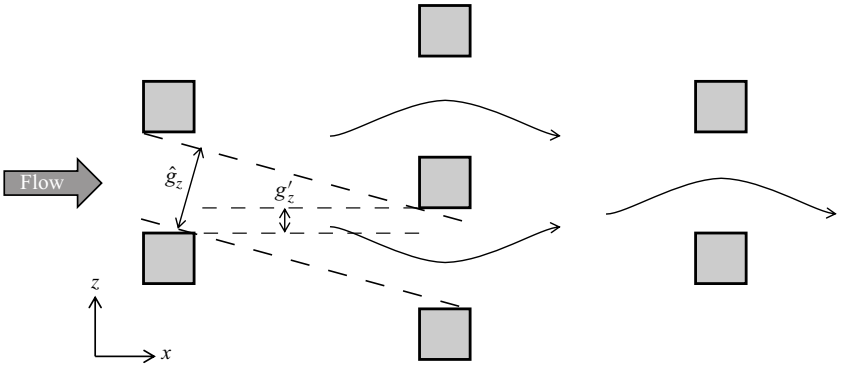


Figure 20. Sketch of a staggered-layout canopy comparing the frontal gap, g_z', and an effective gap reflecting the flow meandering, $\widehat{g}_z^+$.

of meandering in wall turbulent eddies and, in addition, from Taylor's frozen turbulence hypothesis (Taylor 1938) we would expect eddies to loosely follow the path of mean-flow streamlines, which within the canopy meander themselves around the canopy elements. A rigorous calculation of the width for such 'streamline pathways' is in principle possible using the ensemble average flow of (3.2), but in the present first approximation we use the simple, rough estimate of an effective, oblique gap $\widehat{g}_z$, calculated from the canopy geometry alone, as indicated in figure 20. We note that the same oblique gap can also be calculated for x-staggered canopies, but in that case it would be narrower than the g_z of their streamwise-aligned canyons. In general, we would expect the larger of g_z, g_z' and $\widehat{g}_z$ to be the effective gap in terms of eddy penetration, which implicitly entails that, for $\widehat{g}_z$ to be the effective gap, the associated oblique paths must have limited yaw. Figure 21 suggests that $\widehat{g}_z$ is a reasonable approximation for the effective gap for the present z-staggered canopies, which prefigures how to approach the problem for more complex canopy layouts.

https://doi.org/10.1017/jfm.2026.11446 Published online by Cambridge University Press

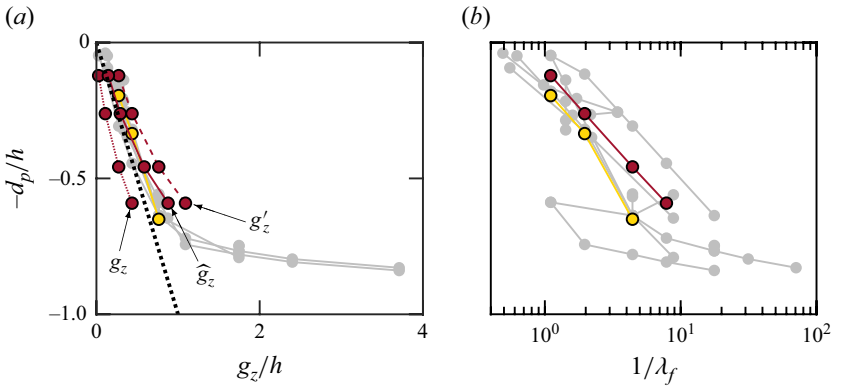


Figure 21. Penetration depth d_p versus spanwise gap g_z and frontal density λ_f, with lengths scaled with the canopy height h. ●, x-staggered canopies 'SX'; ●, z-staggered canopies 'SZ'; ●, cases already portrayed in figure 19. The coloured lines connect cases in the corresponding set; dotted lines connect markers for the original gap from the isotropic layout, g_z; dashed lines markers for the frontal gap, g_z'; solid lines markers for the effective gap, $\widehat{g}_z$, defined in figure 20. The black dotted lines are $d_p = g_z$.

5. Conclusions

In the present work, we have identified and characterised canopy density regimes based on the penetration of eddies from the overlying turbulence. In the sparse regime, turbulence penetrates with little obstruction into the canopy all the way to the canopy floor, whereas in the dense regime, this penetration is limited. We have examined the conventional measure of canopy density using frontal density λ_f, and found that λ_f alone cannot fully characterise canopy density, as it cannot capture e.g. the effect of different streamwise and spanwise spacing of the canopy elements or of the Reynolds number.

To measure turbulence penetration, we focus on flow structures of intense local Reynolds shear stress $u'v'$, as these structures are responsible for momentum transport and turbulence diffusion. We separate overlying-turbulence structures from element-coherent ones by spectral filtering, and choose a suitable $u'v'$ threshold to delimit them through a percolation analysis. We then focus on the structures that are, at least partially, in the immediate vicinity of the canopy-tip plane, referring to them as 'interfacial eddies', and propose metrics to quantify their location, span and volume. We apply these metrics to analyse a series of canopies across a range of frontal densities $\lambda_f \approx 0.01$–2.04, heights $h^+ \approx 44 - 266$ and Reynolds numbers $Re_\tau \approx 180 - 2000$.

Our results show that, for the same λ_f, streamwise-packed canopies with large spanwise gaps allow eddies to penetrate effectively, and thus behave as sparser compared with the corresponding isotropic and spanwise-packed canopies, which limit eddy penetration to a significantly greater degree. Streamwise-packed canopies with frontal densities as high as $\lambda_f \approx 0.9$ still behave as sparse, while only in the limit of very small frontal density, $\lambda_f \lesssim 0.06$, do canopies behave as sparse regardless of their anisotropy, Our results further show that turbulence penetration remains similar when the spanwise gap between canopy elements is fixed, regardless of their pitch (spacing) and width. For closely packed canopies with small spanwise gaps, $g_z^+ \lesssim 15$, turbulence penetration is restricted to a few visocus units. As the spanwise gaps widen, canopies behave increasingly as sparse, allowing eddies to penetrate deeper and more vigorously. This occurs as the eddies are increasingly unhindered as they are advected downstream through the canyons that appear between canopy elements. Turbulence penetration not only depends on the canopy topology, but also on the Reynolds number. A canopy with fixed geometry can

https://doi.org/10.1017/jfm.2026.11446 Published online by Cambridge University Press

inhibit turbulence penetration at low Reynolds numbers, $Re_\tau \approx 180$, when its dimensions in viscous units, mainly g_z^+, are small, but permit increasing penetration as Re_τ and g_z^+ increase. In turn, canopies with the same dimensions in inner units exhibit similar density regimes and penetration depth across different Re_τ.

Overall, our results suggest that turbulence penetration depends on the effective spanwise gap of the canyons between canopy elements, and how it compares with the typical spanwise size of interfacial eddies. The latter scales generally with the zero-plane-displacement depth, resulting in a penetration depth $d_p \sim g_z$ unless further limited by the immediate vicinity of the canopy bed – something that occurs for sparse canopies. This leads to a characterisation of canopy density in terms of d_p/h, the proportion of the canopy that the overlying turbulence can penetrate, as a function of the canyon-width-to-element-height ratio g_z/h. Dense canopies have $g_z/h \lesssim 0.2$, their turbulence penetration is small and follows roughly $d_p \approx g_z$. Intermediate canopies have $0.2 \lesssim g_z/h \lesssim 1$, and experience an eventual departure from $d_p \approx g_z$ for large g_z/h. Sparse canopies have $g_z/h \gtrsim 1$, and their turbulence penetration approaches the full height of the canopy, $d_p/h \approx 0.9$.

The present study has focused on canopies of collocated elements. Nevertheless, preliminary results for staggered layouts suggest that the concept of canyons through which eddies travel can be extended to more complex layouts, which would allow estimates for their effective gap, the degree of eddy penetration and the corresponding density regime.

Funding. This work was supported in part by the UK Engineering and Physical Sciences Research Council (EPSRC) under grant EP/S013083/1. Computational resources were provided by the University of Cambridge Research Computing Service under EPSRC Tier-2 grant EP/P020259/1 (project cs155), and by the UK 'ARCHER2' system under PRACE project pr1u1702 and EPSRC Access to HPC projects e776 and e800. For the purpose of open access, the authors have applied a Creative Commons Attribution (CC BY) licence to any Author Accepted Manuscript version arising from this submission.

Declaration of interests. The authors report no conflicts of interest.

Data availability. All data used in this publication are available within the publication. Raw simulation data can be accessed by contacting the corresponding author with reasonable requests.

Appendix A. Assessment of other density characteristic length scales as predictors for eddy penetration depth

In § 1 we have discussed different length scales that can be used to characterise canopy density, such as the drag length, $\ell_d = (U)^2/D$, the shear length, $\ell_s = U/(\mathrm{d}U/\mathrm{d}y)$ and the turbulent mixing length, $\ell_m = [\overline{u'v'}]^{1/2}/(\mathrm{d}U/\mathrm{d}y)$, all measured at the plane of the canopy tips, or the zero-plane-displacement depth below that plane, d_0. All of these length scales are based on properties of the mean flow, and thus all give a measure of its degree of penetration within the canopy. Throughout the paper, in contrast, we have advocated for characterising the penetration of turbulence in terms of the penetration of turbulent eddies, rather than of the mean velocity profile. Form this, we have proposed the use of the eddy canyon gap g_z as a predictor for eddy penetration and thus canopy density. Figures 19(b) and 21(a) portray the collapse of d_p with g_z, summarising the paper. For comparison, figure 22 portrays results for the above four length scales vs d_p. The scatter observed is significantly larger than for g_z, and comparable to that for the frontal density λ_f, shown for instance in figure 21(b).

Figure 23 portrays results for the mean velocity profile $U(y)$ for a wide variety of canopy layouts, and includes values for d_p for reference. Again, although the shape of the mean velocity profile exhibits a generally monotonic evolution with increasing canopy density, this evolution is not always consistent with that of the penetration depth d_p. This highlights

https://doi.org/10.1017/jfm.2026.11446 Published online by Cambridge University Press

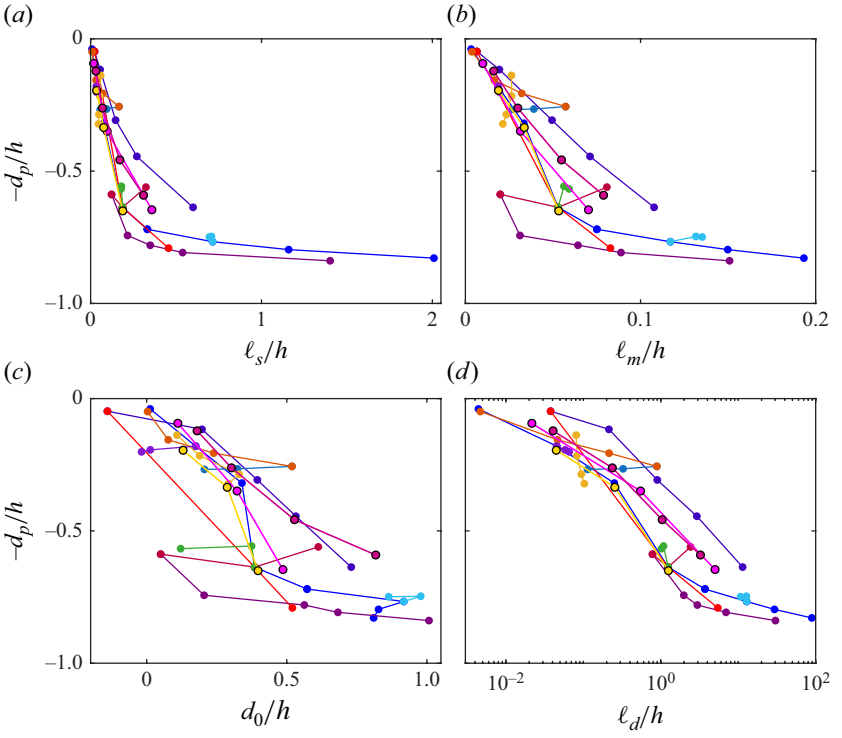


Figure 22. Penetration depth d_p versus (*a*) shear length ℓ_s, (*b*) mixing length ℓ_m, (*c*) zero-plane-displacement depth d_0 and (*d*) drag length ℓ_d, relative to the canopy height h. Canopies are ●, isotropic; ●, 'fence-like'; ●, 'canyon-like' ; ●, fixed s_z; ●, fixed s_x; ●, fixed gap; ●, fixed pitch; ●, 'outer similar' ; ●, ●, and ●, 'inner similar' with $\lambda_f \approx 0.91$, 0.23 and 0.11, respectively; ●, 'doubled height', $h^+ \approx 220$; ●, streamwise staggered; ●, spanwise staggered. The coloured lines connect cases in the corresponding set.

that the coupling between the penetration of the mean velocity and of the turbulence are not completely coupled.

Appendix B. Filtering out the element-coherent flow

This appendix details the spectral filter applied in § 3.1 to remove the element-coherent flow and isolate the background-turbulence eddies. Figure 24 portrays premultiplied spectra, e.g. $k_x k_z E_{uu}$, for the three velocity components and the shear Reynolds stress at various heights above the tip plane for two sample canopies. These maps portray the spectral energy density across different wavelengths (or length scales) in x and z. As shown in figure 24(*a–d*), the element-coherent footprint appears as concentrated energy at the canopy pitch s^+ and its harmonics. This footprint decays naturally with height above the canopy-tip plane, leaving only the background-turbulence wavelengths. Thus, we can use these background wavelengths to construct a spectral filter that selectively removes the element-coherent signal while retaining the background flow field.

To establish this filter, we first identify the height at which the element-coherent signal has decayed naturally. Near the tips, the scale of the element-coherent eddies is generally determined by the element width or gap, which provides the size of the 'active' region for canopy–turbulence interaction (Sharma & García-Mayoral 2020*b*). When the element width is larger than the gap ($w^+ > g^+$), the element-coherent eddies are approximately of

https://doi.org/10.1017/jfm.2026.11446 Published online by Cambridge University Press

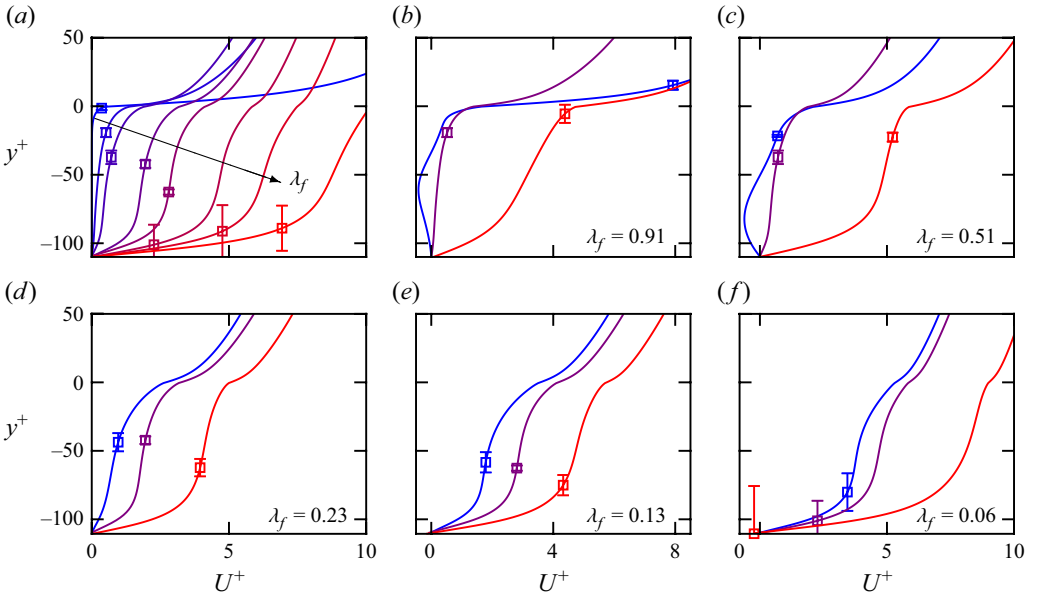


Figure 23. Mean velocity profiles U^+ versus height y^+ for the same canopies of figure 11: (*a*) isotropic layouts with increasing frontal density, from red to blue $\lambda_f \approx 0.01$–2.04; (*b*) through (*f*), fence-like (blue), isotropic (magenta) and canyon-like (red) layouts with $\lambda_f \approx 0.06$–0.91. The symbols and error bars are for the corresponding values of the penetration depth d_p.

the size of the element width (Poggi *et al.* 2004; Sadique *et al.* 2017; Sharma & García-Mayoral 2020*a*). Conversely, when the gap is larger than the element width ($w^+ < g^+$), the element-coherent eddies are approximately of the size of the gap (MacDonald *et al.* 2018). Thus, the reference height for the spectral filter depends on a 'decay length', which characterises the height over which the element-coherent flow vanishes, defined as $\ell_d^+ = min(w^+, g^+)$. For our anisotropic canopies with $s_x \neq s_z$, we use $\ell_d^+ = w^+$ for simplicity. As shown in figure 24, the element-coherent footprint, in the form of spectral spikes at the streamwise and/or spanwise wavelengths of the canopy (Abderrahaman-Elena *et al.* 2019), essentially vanishes at a height of two 'decay lengths', $y^+ \approx 2\ell_d^+ \approx 48$, above both the isotropic canopy $\mathrm{I}_{S216\times216}$ and the fence-like canopy $\mathrm{F}_{S144\times36}$, suggesting that this as a suitable reference height to capture the background signal alone.

As depicted in figure 25(*a*,*e*), the filter removes the energy at the canopy pitch and its harmonics, while retaining the main spectral 'lobe' of background-turbulence wavelengths. The energy within this 'lobe' accounts for 97 % of $(u'^+)^2$ and $(v'^+)^2$, respectively. Care must be taken when choosing this filter percentage because if too many wavelengths remain unfiltered, too little element-coherent flow is removed. However, if too many wavelengths are removed, the background flow within the substrate can be distorted or significantly reduced, artificially removing the signature of the eddies that are actually penetrating.

The spectral filter is applied within the canopy region ($y^+ \leq 0$) to remove the element-coherent flow, while it is switched off at height $y^+ \geqslant 2\ell_d^+$, where the element-coherent flow has already decayed. To avoid an abrupt transition, we apply a half-Hanning window for the filter intensity at height $0 \leqslant y^+ \leqslant 2\ell_d^+$, gradually reducing the filtered energy from 100 % at $y^+ \leq 0$ to 0 % at $y^+ \geq 2\ell_d^+$ for each filtered wavelength. As illustrated in figure 25, the proposed filter removes the energy in the canopy harmonics and the

https://doi.org/10.1017/jfm.2026.11446 Published online by Cambridge University Press

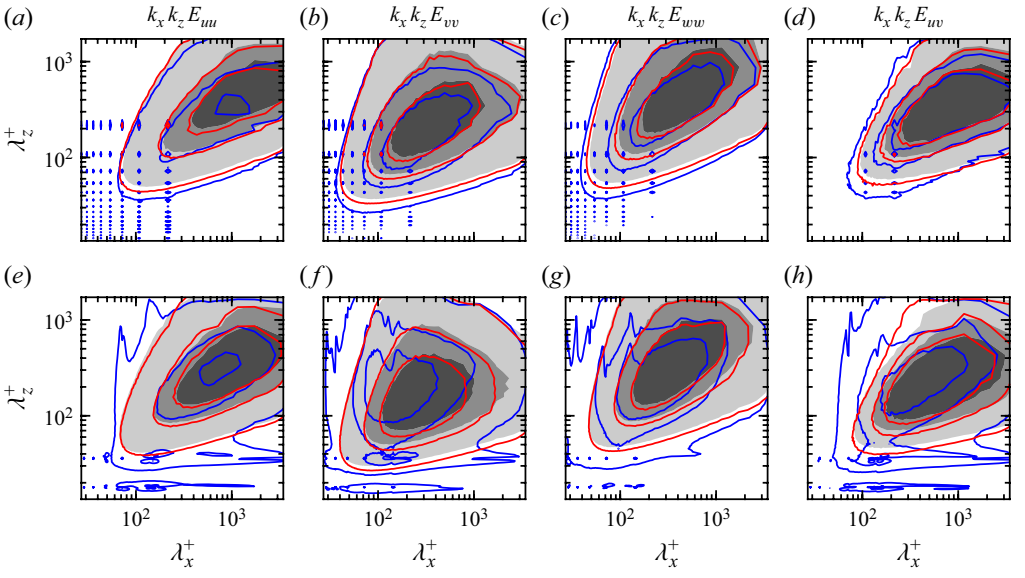


Figure 24. Spectral energy densities versus streamwise and spanwise wavelengths λ_x^+ and λ_z^+; (*a–d*) case $\mathrm{I}_{S216\times216}$; (*e–h*) case $\mathrm{F}_{S144\times36}$. The blue, red and shaded contours are at heights $y = (0, 1, 2)\,\ell_d$ above the tips, respectively, where $l_d^+ = w^+ \approx 24$. The contours are at 0.01, 0.05 and 0.1 times the root-mean-square (r.m.s.) level.

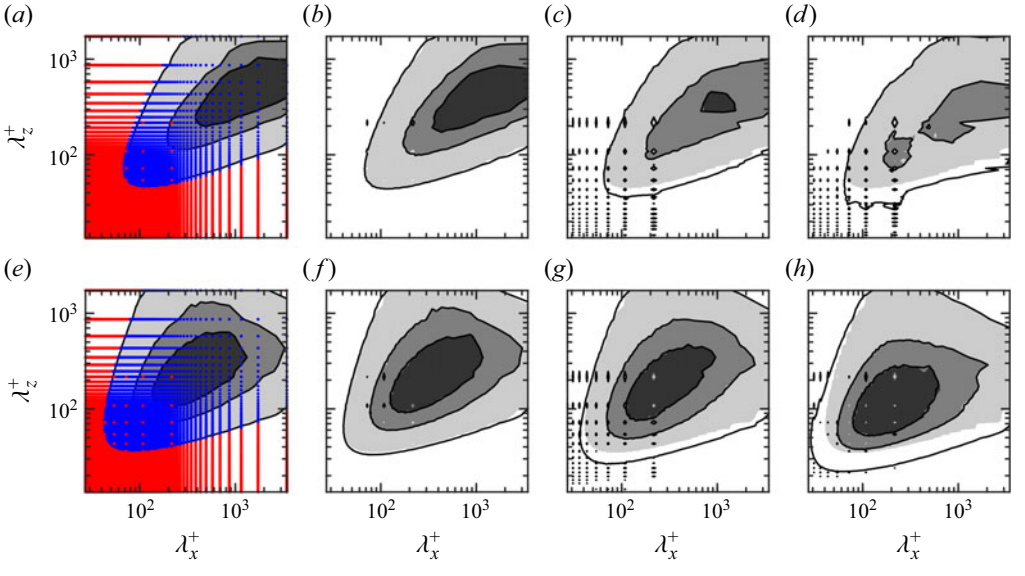


Figure 25. Spectral filters and spectral energy densities versus streamwise and spanwise wavelengths λ_x^+ and λ_z^+ for case $\mathrm{I}_{S216\times216}$. Panels show (*a–d*) $k_x k_z E_{uu}$; (*e–h*) $k_x k_z E_{vv}$. Contours from left to right represent energy densities at $y^+ \approx 48$, 24, 0 and -55. Line contours represent the energy density of the raw velocity, and shaded contours that of the filtered flow fields. The filters are shown in (*a*, *e*), where red dots indicate the wavelengths filtered out and blue dots those retained, containing up to 97 % of the total $(u'^+)^2$ and $(v'^+)^2$, respectively. The contour levels are 0.01, 0.05 and 0.1 times the r.m.s. level.

https://doi.org/10.1017/jfm.2026.11446 Published online by Cambridge University Press

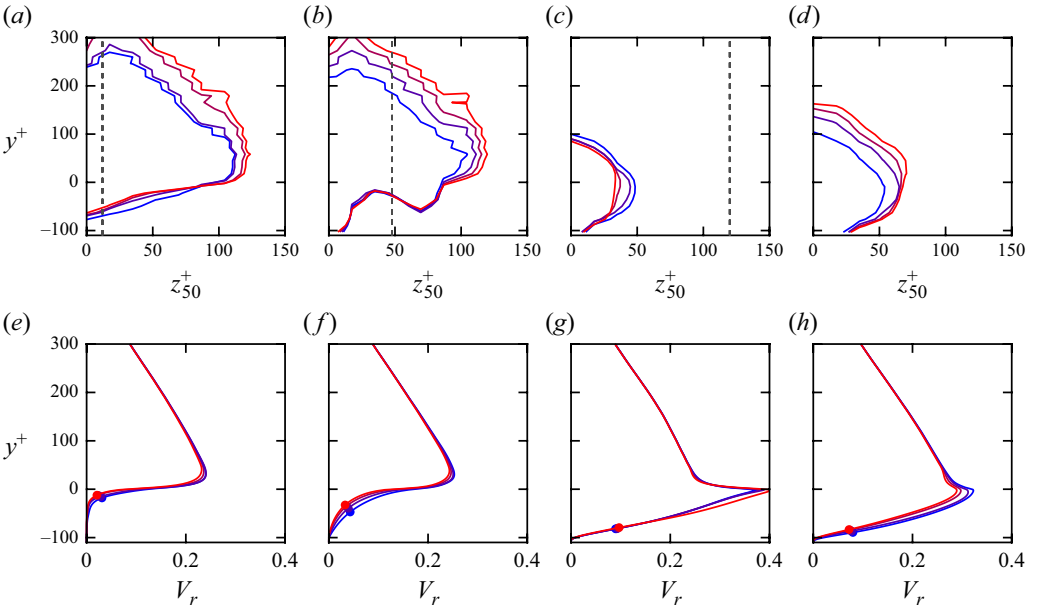


Figure 26. Characteristic spanwise width z^+_{50} and relative volume V_r at each height y^+ for different levels of filtering. From blue to red, the contours are for filter levels 100 % (no filter), 99 %, 97 % and 95 %. Cases portrayed are (*a*,*e*) $\mathrm{Fs}_{144\times36}$; (*b*,*f*) $\mathrm{Is}_{72\times72}$; (*c*, *g*) $\mathrm{Cs}_{36\times144}$; (*d*,*h*) $\mathrm{Is}_{216\times216}$. In (*a–d*), the p.d.f. contours enclose 75 % of the penetrating eddies, and the dashed lines mark the corresponding inter-element gap $g_z^+ \approx 12$, 48, 120 and 192, when within the range displayed. In (*e–h*), markers • indicate the penetration depth where $V_r / V_{r,tip} = 0.25$.

quiescent wavelengths. We note that this also removes any background-turbulence signal that may exist at the canopy harmonics, but this contribution is generally small compared with the remainder.

The filter intensity must be chosen carefully so that the background eddies are not eliminated or significantly distorted. Figure 25(*a*,*e*) shows that, for the filter applied throughout the paper, the filtered flow retained 97 % of the total energy of the turbulent fluctuations $(u'^+)^2$ and $(v'^+)^2$. Here, we assess the sensitivity of the filtered $u'v'$ structures by comparing results based on filter levels that retain 100 % (no filter), 99 %, 97 % and 95 % of the fluctuating energy. The goal is to ensure that the location and topology of the background-turbulence structures remain consistent regardless of the filter intensity, while the element-coherent signal is effectively removed. Results are shown in figure 26(*a–d*), where the characteristic width z^+_{50} at each height of eddies within the canopy remains similar across all filter levels. The collapse of the relative volume V_r and the penetration depth d_p^+, shown in figure 26(*e–h*), further confirms that the applied filter essentially isolates the background turbulence without altering it significantly. As illustrated in figure 27, both the stem-scale wakes behind the elements in panel (*a*) and the shedding eddies between the fences in panel (*b*) are effectively removed for filter levels ≤ 99 %, while the background-turbulence structures remain mostly unaffected.

Appendix C. Determining the extent of $u'v'$ eddies

This appendix details the methodology used to set the threshold value used in (3.3) to determine the extent in space of the structures of intense point-wise $u'v'$ from the

https://doi.org/10.1017/jfm.2026.11446 Published online by Cambridge University Press

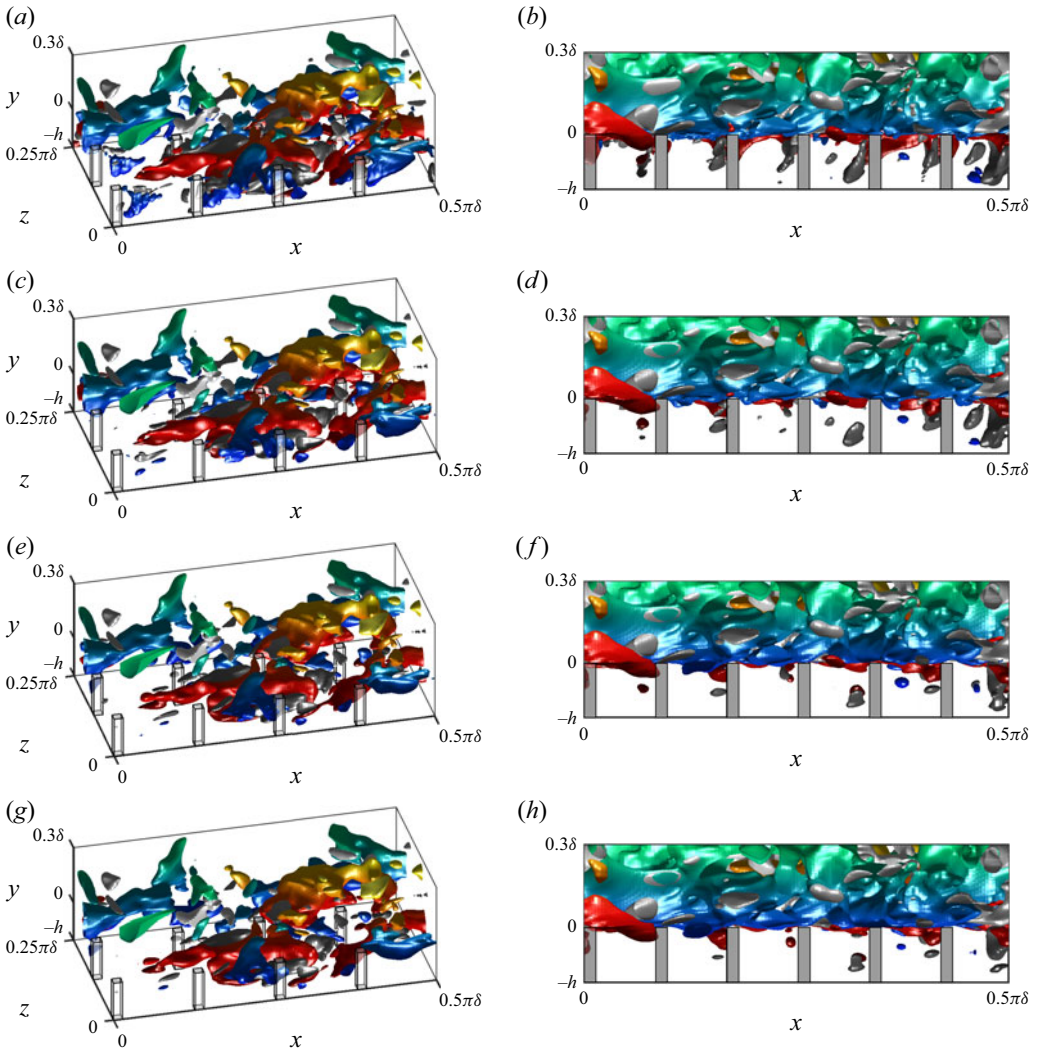


Figure 27. Instantaneous realisations of $u'v'$ structures for canopies $I_{S216\times216}$ (*a*,*c*,*e*,*g*) and $F_{S144\times36}$ (*b*,*d*,*f*,*h*). The filter levels are 100 % (no filter) in (*a*,*b*), 99 % in (*c*,*d*), 97 % in (*e*,*f*) and 95 % in (*g*,*h*). The structures are coloured by distance to the floor, ejections blue to green, sweeps red to yellow, and outward and inward interactions grey to white.

background turbulence that come into contact with the canopy. The choice of the right-hand side in (3.3) can significantly influence the resulting topology of the eddies. A low threshold value results in large, interconnected eddies spanning the entire flow field, while an excessively high threshold may filter out too many actual eddies, leaving a thin skeleton for only the most intense ones (Nagaosa & Handler 2003; Del Alamo *et al.* 2006). In smooth-wall studies, three-dimensional flow structures are typically identified using height-dependent normalisation factors to reflect the intense variation of mean shear Reynolds stress with height (Jiménez 2018; Marusic & Monty 2019). The early work of quadrant analysis by Willmarth & Lu (1972) used the mean Reynolds shear stress at each height $|\overline{u'v'(y)}|$

$$|u'v'(x,\,y,\,z)| > H_{u'v'(y)}|\overline{u'v'(y)}|. \tag{C1}$$

https://doi.org/10.1017/jfm.2026.11446 Published online by Cambridge University Press

However, this approach encounters a limitation when $|\overline{u'v'(y)}|$ tends toward zero near the channel centre, leading to an exaggerated representation of the eddies in this region. This limitation could be circumvented by using the r.m.s. of velocity fluctuations $u'(y)$ and $v'(y)$, as in Wallace, Eckelmann & Brodkey (1972), Lu & Willmarth (1973) and Bogard & Tiederman (1986), or the r.m.s. of Reynolds stress fluctuation (Narasimha *et al.* 2007). In the present case, the height-dependent normalisation factors $|\overline{u'v'(y)}|$, $u'(y)v'(y)$ and $(uv)'(y)$ decrease rapidly with depth into the canopy, which would result in an over-representation of the eddies within. Sharma & García-Mayoral (2020*b*) reported that turbulent fluctuations decayed exponentially within the canopy, with the slowest decay occurring for the wall-normal component v', even when persistent footprints of Kelvin–Helmholtz rollers were still observed at half-height below the tips for dense canopies. Consequently, as the above height-dependent normalisation factors become vanishingly small within a dense canopy, weak fluctuations would be identified as strong eddies, with their significance overemphasised. To avoid this, we normalise the pointwise Reynolds shear stress with a y-constant value, as indicated in (3.3), using the total shear stress at the canopy-tip plane, τ_{tip}. This normalisation factor allows a consistent statistical analysis of canopies across various density regimes using a constant H, circumventing the need to recalibrate the value of H for each canopy, as τ_{tip} provides the scale for the flow in the vicinity of the tips for both dense and sparse canopies. In contrast, alternative normalisation factors, such as $u'v'(y_{tip})$ and $u'(y_{tip})v'(y_{tip})$, can yield large values for H for dense canopies and small values for sparse canopies, complicating the comparative analysis across different canopies.

The value of the threshold H in (3.3) is determined based on a percolation analysis (Del Alamo *et al.* 2006), as depicted in figure 28. This percolation analysis examines how the size and connectivity between identified eddies vary as a function of H. At high values of H ($H \gtrsim 3$), only a few eddies, corresponding to the core of the most intense structures, are identified. As H decreases, new structures are identified while the existing ones expand in size. For $H \lesssim 3$, the largest eddy expands proportionally with the total volume, and the volume ratio between the largest eddy and all eddies, $V_{largest}/V_{total}$, remains roughly constant. As H continues to decrease, the identified objects begin to merge, significantly increasing the ratio $V_{largest}/V_{total}$. For $H \lesssim 1$, the total number of eddies, normalised with its maximum, N/N_{max} decreases, and $V_{largest}/V_{total}$ approaches unity as most eddies merge into a single one. This sudden transition is the percolation crisis, at which separate turbulent structures coalesce into one large connected cluster, and the distinction between individual eddies is lost (Del Alamo *et al.* 2006). Figure 28 illustrates that a percolation crisis occurs when $0.5 \lesssim H \lesssim 3$ for all cases. We therefore use $H = 1.6$ throughout to ensure that individual structures remain separate while avoiding excessive volume shrinkage.

For H within the range of the percolation crisis, the size and location of the penetrating eddies are largely insensitive to the exact choice of H. Although the eddy volume at each height increases slightly for larger H, the penetration depth remains unaffected. We assess this by comparing results with thresholds $H = 1.2, 1.6, 2.0$. As H decreases, new structures emerge while the existing ones expand in size, leading to a slight increase in the relative volume V_r at each height, as shown in figure 29(*e–h*). Nevertheless, the penetration depth d_p^+ remains consistent across all examined values of H. Similarly, figure 29(*a–d*) shows that the characteristic spanwise width z_{50}^+ at each height within and immediately above the canopies are similar for different H, and only exhibit differences far above the canopy-tip plane. We can conclude that the influence of the choice of H in the range $H = 1.2$–2 has no significant influence on our results and the ensuing conclusions.

https://doi.org/10.1017/jfm.2026.11446 Published online by Cambridge University Press

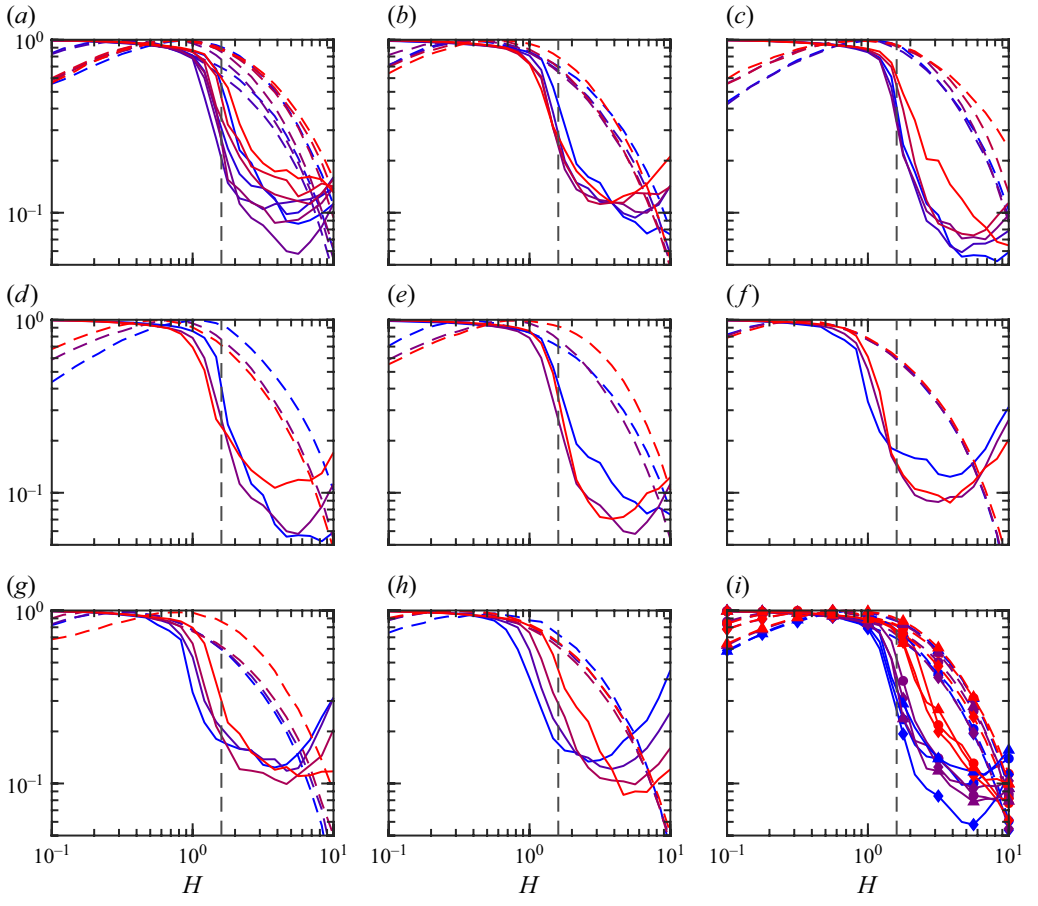


Figure 28. Percolation diagrams for the identification of $u'v'$ structures for a broad set of canopies as a function of the threshold value H in (3.3). Solid lines represent the volume ratio between the largest eddy and the total volume of all eddies, $V_{largest}/V_{total}$; dashed lines represent the ratio of the number of identified eddies to the maximum number of eddies, N/N_{max}: (*a*) canopies with isotropic layout; (*b*) fence-like layout; (*c*) canyon-like layout; (*d*) fixed s_z; (*e*) fixed s_x; (*f*) fixed gap; (*g*) fixed pitch; (*h*) similar geometry in outer units; and (*i*) similar geometry in inner units. From blue to red, the lines represent canopies with decreasing λ_f in (*a–g*) and increasing Re_τ in (*h,i*). In (*i*), the symbols ●, ♦ and ▲, mark the cases with the same geometry as $\mathrm{IS550}_{\mathrm{G30\times30}}$, $\mathrm{IS550}_{\mathrm{G84\times84}}$ and $\mathrm{IS550}_{\mathrm{G192\times192}}$, respectively. The chosen threshold $H = 1.6$ is indicated by a vertical dashed line.

Appendix D. Quadrant-wise analysis of eddy penetration

The analysis of structures of intense pointwise Reynolds stress $u'v'$ can also distinguish between structures in different quadrants, depending on the signs of the fluctuating velocity components u' and v' (Wallace *et al.* 1972; Willmarth & Lu 1972; Lozano-Durán *et al.* 2012; Lozano-Durán & Jiménez 2014). The quadrants Q1, Q2, Q3 and Q4 represent outward interactions ($u' > 0$, $v' > 0$), ejections ($u' < 0$, $v' > 0$), inward interactions ($u' < 0$, $v' < 0$) and sweeps ($u' > 0$, $v' < 0$), respectively. Depending on the density regime, turbulent structures from different quadrants can have different intensities and locations (Brunet 2020).

Figure 30 depicts the typical spanwise size z_{50}^+ at each height of eddies across all four quadrants for isotropic-layout canopies with $s^+ \approx 35$, 70 and 430, using the same contour level used in figure 8 for all $u'v'$ structures together. This analysis provides insights into

https://doi.org/10.1017/jfm.2026.11446 Published online by Cambridge University Press

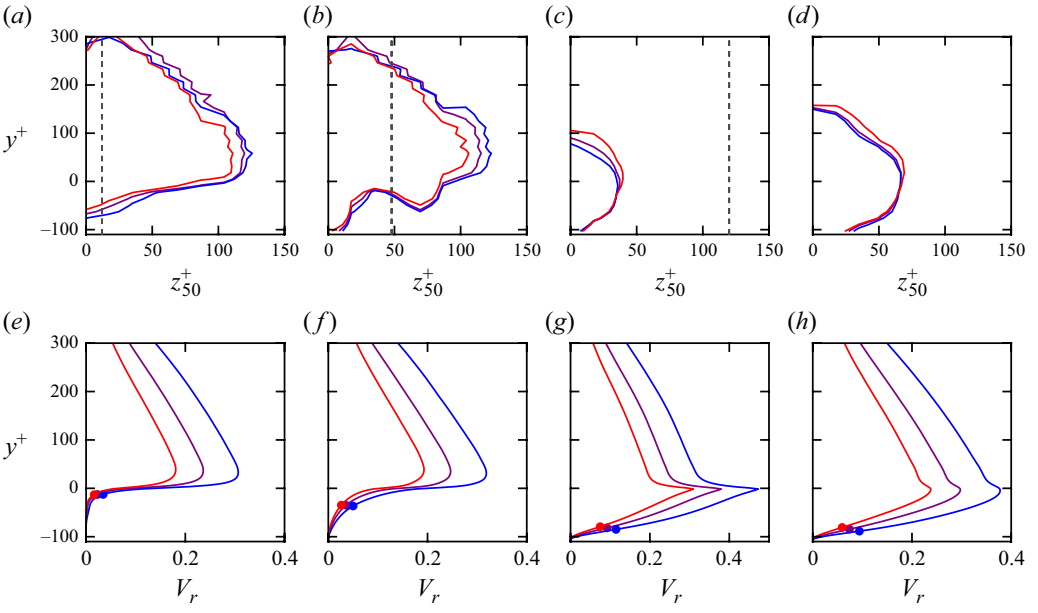


Figure 29. Characteristic spanwise width z^+_{50} and relative volume V_r at each height y^+ for different values of the threshold H in (3.3). From blue to red, thresholds $H = 1.2$, 1.6 and 2.0. Cases portrayed are (*a*,*e*) $\mathrm{Fs}_{144\times36}$; (*b*,*f*) $\mathrm{Is}_{72\times72}$; (*c*, *g*) $\mathrm{Cs}_{36\times144}$; (*d*,*h*) $\mathrm{Is}_{216\times216}$. In (*a–d*) the p.d.f. contours enclose 75 % of the penetrating eddies, and the dashed lines mark the corresponding inter-element gap, $g^+_z \approx 12$, 48, 120 and 192, when within the range displayed. In (*e–h*), markers • indicate the penetration depth where $V_r / V_{r,tip} = 0.25$.

how structures from different quadrants, e.g. sweeps and ejections, penetrate differently. For the dense canopy $\mathrm{Is}_{36\times36}$, sweeps dominate the turbulent structures. This is expected because the stress balance in a turbulent channel requires $\overline{u'v'} < 0$, which enhances the significance of sweeps and ejections with $u'v' < 0$. Furthermore, near the canopy-tip plane, ejections and outward interactions with $v' > 0$ are significantly hindered by the canopy drag (Huang *et al.* 2009; Sharma & García-Mayoral 2020*b*). As a result, only large sweeping structures are observed to penetrate slightly into the dense canopy with very few ejections springing out of it. For the intermediate canopy, sweeps and ejections exhibit larger spanwise widths and occur more frequently than inward and outward interactions. The dominance of sweeps and ejections within and above vegetation canopies has long been recognised, from early studies such as Nakagawa & Nezu (1977), Finnigan (1979) and Raupach & Thom (1981), to later works including Gardiner (1994), Novak *et al.* (2000) and Dupont *et al.* (2010), consistent with our observations. These studies noted that sweeps generally contribute more significantly to Reynolds shear stress compared with ejections. Finally, for a sparse canopy like $\mathrm{Is}_{432\times432}$, structures from different quadrants exhibit similar spanwise widths and occur with comparable frequency, suggesting a more uniform contribution from all four quadrants.

Figure 31 portrays the characteristic streamwise x^+_{50} and spanwise z^+_{50} sizes at each height of structures in different quadrants for the canopies discussed in § 4.2, with fixed element geometry and pitch in one direction and varying pitch in the other. Panels (*a–d*) show that canopies with a fixed spanwise pitch $s^+_z \approx 108$ allow turbulence to penetrate effectively into the canopy, and the eddies within can elongate up to $x^+_{50} \approx 120$, with no significant influence of the value of s^+_x. However, in contrast to these fixed-s_z canopies, where turbulence penetration is largely unimpeded, canopies with a constant streamwise

https://doi.org/10.1017/jfm.2026.11446 Published online by Cambridge University Press

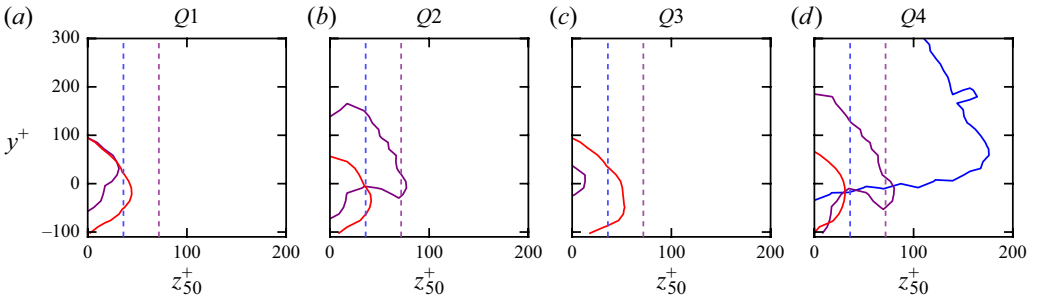


Figure 30. P.d.f. of the spanwise width z_{50}^+ vat each height y^+ of interfacial eddies from different $u'v'$ quadrants. Blue contours are for dense canopy $\mathrm{I}_{S36\times36}$, magenta contours for intermediate canopy $\mathrm{I}_{S72\times72}$ and red contours for sparse canopy $\mathrm{I}_{S432\times432}$. The dashed vertical lines mark the corresponding element pitch $s^+ \approx 36$, 72 and 432, with the latter beyond the abscissa range displayed. The contour level for each canopy encloses 75 % of the eddies from the corresponding quadrant. In (*a–c*), the occurrence of interfacial eddies of canopy $\mathrm{I}_{S36\times36}$ is too low to be captured.

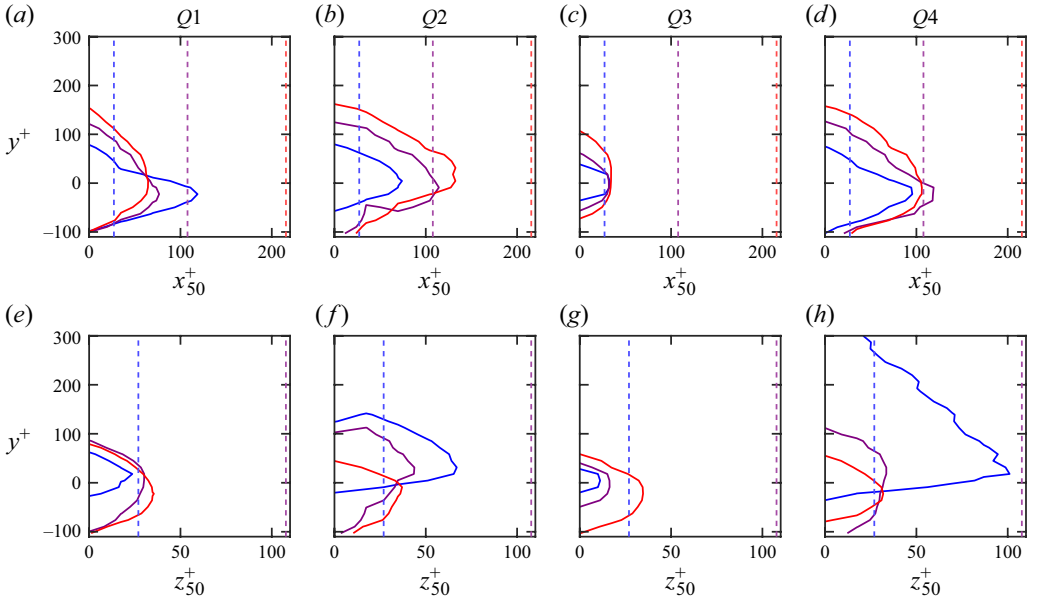


Figure 31. P.d.f. of the characteristic wall-parallel sizes x_{50}^+ and z_{50}^+ at each height y^+ of interfacial eddies from different quadrants. (*a–d*) Eddy streamwise length for canopies with a fixed $s_z^+ \approx 108$; (*e–h*) eddy spanwise width for canopies with a fixed $s_x^+ \approx 108$. The blue, purple and red contours are for canopies with frontal densities $\lambda_f \approx 0.91$, 0.23 and 0.11, respectively; the dashed lines mark the canopy streamwise and spanwise pitch, s_x^+, $s_z^+ \approx 27$, 108 and 216. The contours enclose 75 % of all eddies.

pitch $s_x^+ \approx 108$ exhibit different penetration behaviours depending on their spanwise pitch, as illustrated in figure 31(*e–h*). A fence-like canopy such as $\mathrm{X}_{S108\times27}$ significantly restricts turbulence penetration, allowing limited Q2 and Q4 structures to penetrate, with Q4 structures having the highest occurrence and the largest width, up to $z_{50}^+ \approx 100$. This suggests that sweeps dominate turbulence penetration within fence-like canopies, which is consistent with previous observations on obstructing vegetation canopies (Poggi *et al.* 2004; Yue *et al.* 2007; Bailey & Stoll 2013). Bailey & Stoll (2013) reported that the dominance of sweeps persists even when the streamwise pitch between the fences increases

https://doi.org/10.1017/jfm.2026.11446 Published online by Cambridge University Press

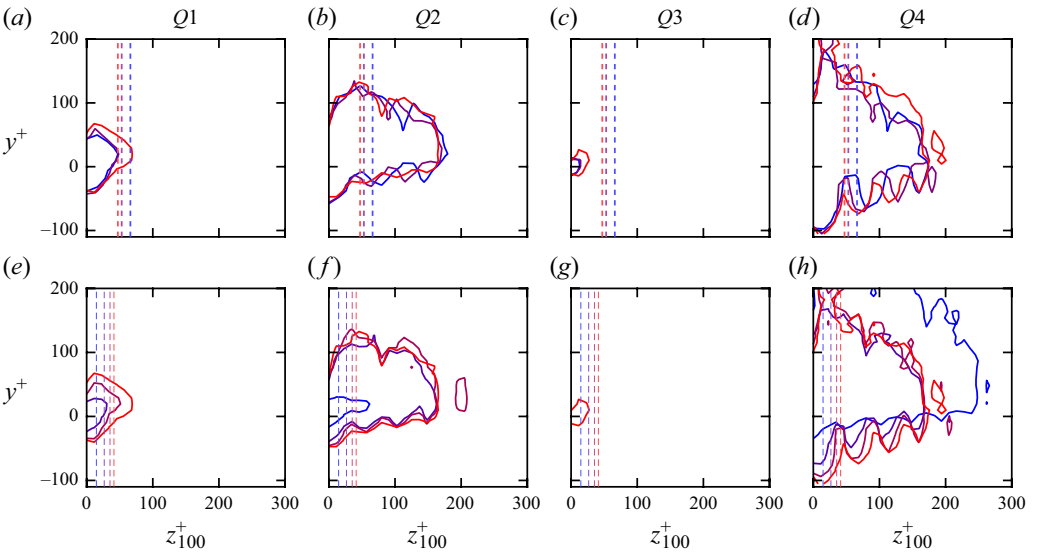


Figure 32. P.d.f. of the total spanwise width z^+_{100} at each height y^+ of eddies from different $u'v'$ quadrants, for canopies with (*a–d*) fixed gap $g_z^+ \approx 41$ and (*e–h*) fixed pitch $s_z^+ \approx 47$. Colours and contour levels are as in figure 14.

to $s_x/h \approx 3$. In contrast, as s_z^+ increases, canopies such as $\mathrm{X_{S108\times108}}$ and $\mathrm{X_{S108\times216}}$ allow turbulence to penetrate more effectively, and structures in different quadrants have a more uniform contribution to turbulence penetration.

In turn, figure 32 illustrates the relative contributions from different quadrants to the overall turbulence penetration for the canopies discussed in § 4.3, with either a fixed element gap and varying pitch or fixed pitch and varying gap. For all the canopies portrayed, sweeps and ejections dominate the penetrating structures, and sweeps are generally more intense and penetrate deeper within the canopy compared with ejections. This observation aligns with the findings by Collineau & Brunet (1993), who investigated flows over an obstructing pine forest and found that the ratio of the total stress fraction transferred by sweeps to that transferred by ejections is up to 2 or 3 at height $y/h \approx 0.8$. The dominance of sweeps has also been reported on other obstructing vegetation canopies (Novak *et al.* 2000; Dupont *et al.* 2011; Dupont & Patton 2012), as summarised in Brunet (2020). Figure 32(*d*,*h*) shows that large sweep-type eddies with width $z^+_{100} > g_z^+$ cannot fully enter the canopy, but their 'feet' may partially penetrate if they fit within the gap between elements. As an example, for canopy $\mathrm{S47_{G41\times41}}$ in figure 32(*h*), for large eddies that span multiple canopy elements, their width z^+_{100} exhibits harmonics of the element pitch $s_z^+ \approx 47$ within the canopy. Eddies with increasing widths $z^+_{100} \approx 70, 115, 160$ have decreasing penetration depths $y^+ \approx 75, 60, 40$, respectively, demonstrating a reduced penetration depth for larger footprints.

References

Abderrahaman-Elena, N., Fairhall, C.T. & García-Mayoral, R. 2019 Modulation of near-wall turbulence in the transitionally rough regime. *J. Fluid Mech.* **865**, 1042–1071.

Akbari, H. & Kolokotsa, D. 2016 Three decades of urban heat islands and mitigation technologies research. *Energy Build.* **133**, 834–842.

https://doi.org/10.1017/jfm.2026.11446 Published online by Cambridge University Press

ARSHAD, A., ALI, H.M., ALI, M. & MANZOOR, S. 2017 Thermal performance of phase change material (PCM) based pin-finned heat sinks for electronics devices: effect of pin thickness and PCM volume fraction. *Appl. Therm. Engng* **112**, 143–155.

BAILEY, B.N. & STOLL, R. 2013 Turbulence in sparse, organized vegetative canopies: a large-eddy simulation study. *Boundary-Layer Meteorol.* **147**, 369–400.

BALDOCCHI, D.D. 2003 Assessing the eddy covariance technique for evaluating carbon dioxide exchange rates of ecosystems: past, present and future. *Glob. Change Biol.* **9** (4), 479–492.

BELCHER, S.E. 2005 Mixing and transport in urban areas. *Phil. Trans. R. Soc. Lond. A* **363**, 2947–2968.

BELCHER, S.E., HARMAN, I.N. & FINNIGAN, J.J. 2012 The wind in the willows: flows in forest canopies in complex terrain. *Annu. Rev. Fluid Mech.* **44**, 479–504.

BERRY, P.M., STERLING, M., SPINK, J.H., BAKER, C.J., SYLVESTER-BRADLEY, R., MOONEY, S.J., TAMS, A.R. & ENNOS, A.R. 2004 Understanding and reducing lodging in cereals. *Adv. Agron.* **84** (04), 215–269.

BLOCKEN, B. 2015 Computational fluid dynamics for urban physics: importance, scales, possibilities, limitations and ten tips and tricks towards accurate and reliable simulations. *Build. Environ.* **91**, 219–245.

BOGARD, D.G. & TIEDERMAN, W.G. 1986 Burst detection with single-point velocity measurements. *J. Fluid Mech.* **162**, 389–413.

BREUGEM, W.P., BOERSMA, B.J. & UITTENBOGAARD, R.E. 2006 The influence of wall permeability on turbulent channel flow. *J. Fluid Mech.* **562**, 35–72.

BRITTER, R.E. & HANNA, S.R. 2003 Flow and dispersion in urban areas. *Annu. Rev. Fluid Mech.* **35**, 469–496.

BRUNET, Y. 2020 Turbulent flow in plant canopies: historical perspective and overview. *Boundary-Layer Meteorol.* **177**, 315–364.

CAVA, D. & KATUL, G.G. 2008 Spectral short-circuiting and wake production within the canopy trunk space of an alpine hardwood forest. *Boundary-Layer Meteorol.* **126**, 415–431.

CHAN, L., MACDONALD, M., CHUNG, D., HUTCHINS, N. & OOI, A. 2015 A systematic investigation of roughness height and wavelength in turbulent pipe flow in the transitionally rough regime. *J. Fluid Mech.* **771**, 743–777.

CHEER, A.Y.L. & KOEHL, M.A.R. 1987 Paddles and rakes: fluid flow through bristled appendages of small organisms. *J. Theor. Biol.* **129** (1), 17–39.

CHEN, Z. & GARCÍA-MAYORAL, R. 2023 Examination of outer-layer similarity in wall turbulence over obstructing surfaces. *J. Fluid Mech.* **973**, A31.

COLLINEAU, S. & BRUNET, Y. 1993 Detection of turbulent coherent motions in a forest canopy part II: time-scales and conditional averages. *Boundary-Layer Meteorol.* **66**, 49–73.

CUI, J., PATEL, V.C. & LIN, C.-L. 2003 Large-eddy simulation of turbulent flow in a channel with rib roughness. *Intl J. Heat Fluid Flow* **24** (3), 372–388.

DE LANGRE, E. 2008 Effects of wind on plants. *Annu. Rev. Fluid Mech.* **40**, 141–168.

DEL ALAMO, J.C., JIMÉNEZ, J., ZANDONADE, P. & MOSER, R.D. 2006 Self-similar vortex clusters in the turbulent logarithmic region. *J. Fluid Mech.* **561**, 329–358.

DUPONT, S., BONNEFOND, J.-M., IRVINE, M.R., LAMAUD, E. & BRUNET, Y. 2011 Long-distance edge effects in a pine forest with a deep and sparse trunk space: in situ and numerical experiments. *Agric. Forest Meteorol.* **151** (3), 328–344.

DUPONT, S., GOSSELIN, F., PY, C., DE LANGRE, E., HEMON, P. & BRUNET, Y. 2010 Modelling waving crops using large-eddy simulation: comparison with experiments and a linear stability analysis. *J. Fluid Mech.* **652**, 5–44.

DUPONT, S. & PATTON, E.G. 2012 Influence of stability and seasonal canopy changes on micrometeorology within and above an orchard canopy: the CHATS experiment. *Agric. Forest Meteorol.* **157**, 11–29.

ENDRIKAT, S., MODESTI, D., GARCÍA-MAYORAL, R., HUTCHINS, N. & CHUNG, D. 2021 Influence of riblet shapes on the occurrence of Kelvin–Helmholtz rollers. *J. Fluid Mech.* **913**, A37.

ESCOBEDO, F.J., KROEGER, T. & WAGNER, J.E. 2011 Urban forests and pollution mitigation: analyzing ecosystem services and disservices. *Environ. Pollut.* **159** (8–9), 2078–2087.

FINNIGAN, J. 2000 Turbulence in plant canopies. *Annu. Rev. Fluid Mech.* **32**, 519–571.

FINNIGAN, J.J. 1979 Turbulence in waving wheat: II. Structure of momentum transfer. *Boundary-Layer Meteorol.* **16** (2), 213–236.

FINNIGAN, J.J., SHAW, R.H. & PATTON, E.G. 2009 Turbulence structure above a vegetation canopy. *J. Fluid Mech.* **637**, 387–424.

FLORES, O. & JIMÉNEZ, J. 2010 Hierarchy of minimal flow units in the logarithmic layer. *Phys. Fluids* **22** (7), 071704.

https://doi.org/10.1017/jfm.2026.11446 Published online by Cambridge University Press

García-Mayoral, R. & Jiménez, J. 2011 Hydrodynamic stability and breakdown of the viscous regime over riblets. *J. Fluid Mech.* **678**, 317–347.
Gardiner, B.A. 1994 Wind and wind forces in a plantation spruce forest. *Boundary-Layer Meteorol.* **67**, 161–186.
Huang, J., Cassiani, M. & Albertson, J.D. 2009 The effects of vegetation density on coherent turbulent structures within the canopy sublayer: a large-eddy simulation study. *Boundary-Layer Meteorol.* **133**, 253–275.
Janhäll, S. 2015 Review on urban vegetation and particle air pollution–deposition and dispersion. *Atmos. Environ.* **105**, 130–137.
Jiménez, J. 2012 Cascades in wall-bounded turbulence. *Annu. Rev. Fluid Mech.* **44**, 27–45.
Jiménez, J. 2018 Coherent structures in wall-bounded turbulence. *J. Fluid Mech.* **842**, P1.
Jiménez, J. 2013 Near-wall turbulence. *Phys. Fluids* **25** (10), 101302.
Jiménez, J. & Moin, P. 1991 The minimal flow unit in near-wall turbulence. *J. Fluid Mech.* **225**, 213–240.
Kaimal, J.C. & Finnigan, J.J. 1994 *Atmospheric Boundary Layer Flows: Their Structure and Measurement*. Oxford University Press.
Kim, H., Kline, S.J. & Reynolds, W.C. 1971 The production of turbulence near a smooth wall in a turbulent boundary layer. *J. Fluid Mech.* **50** (1), 133–160.
Kline, S.J., Reynolds, W.C., Schraub, F.A. & Runstadler, P.W. 1967 The structure of turbulent boundary layers. *J. Fluid Mech.* **30** (4), 741–773.
Lightbody, A.F. & Nepf, H.M. 2006 Prediction of velocity profiles and longitudinal dispersion in salt marsh vegetation. *Limnol. Oceanogr.* **51** (1), 218–228.
Ligrani, P.M., Oliveira, M.M. & Blaskovich, T. 2003 Comparison of heat transfer augmentation techniques. *AIAA J.* **41** (3), 337–362.
Lozano-Durán, A., Flores, O. & Jiménez, J. 2012 The three-dimensional structure of momentum transfer in turbulent channels. *J. Fluid Mech.* **694**, 100–130.
Lozano-Durán, A. & Jiménez, J. 2014 Time-resolved evolution of coherent structures in turbulent channels: characterization of eddies and cascades. *J. Fluid Mech.* **759**, 432–471.
Lu, S.S. & Willmarth, W.W. 1973 Measurements of the structure of the Reynolds stress in a turbulent boundary layer. *J. Fluid Mech.* **60** (3), 481–511.
Luchini, P. 2018 Structure and interpolation of the turbulent velocity profile in parallel flow. *Eur. J. Mech. B Fluids* **71**, 15–34.
Luchini, P. 2024 The open channel in a uniform representation of the turbulent velocity profile across all parallel geometries. *J. Fluid Mech.* **979**, R1.
Luhar, M., Rominger, J. & Nepf, H. 2008 Interaction between flow, transport and vegetation spatial structure. *Environ. Fluid Mech.* **8**, 423–439.
MacDonald, M., Ooi, A., García-Mayoral, R., Hutchins, N. & Chung, D. 2018 Direct numerical simulation of high aspect ratio spanwise-aligned bars. *J. Fluid Mech.* **843**, 126–155.
Malhi, Y. 2002 Carbon in the atmosphere and terrestrial biosphere in the 21st century. *Phil. Trans. R. Soc. Lond. A* **360**, 2925–2945.
Marusic, I. & Monty, J.P. 2019 Attached eddy model of wall turbulence. *Annu. Rev. Fluid Mech.* **51**, 49–74.
Mittal, R. & Iaccarino, G. 2005 Immersed boundary methods. *Annu. Rev. Fluid Mech.* **37**, 239–261.
Monti, A., Omidyeganeh, M., Eckhardt, B. & Pinelli, A. 2020 On the genesis of different regimes in canopy flows: a numerical investigation. *J. Fluid Mech.* **891**, A9.
Mousa, M.H., Miljkovic, N. & Nawaz, K. 2021 Review of heat transfer enhancement techniques for single phase flows. *Renew. Sustainable Energy Rev.* **137**, 110566.
Nagaosa, R. & Handler, R.A. 2003 Statistical analysis of coherent vortices near a free surface in a fully developed turbulence. *Phys. Fluids* **15** (2), 375–394.
Nakagawa, H. & Nezu, I. 1977 Prediction of the contributions to the Reynolds stress from bursting events in open-channel flows. *J. Fluid Mech.* **80** (1), 99–128.
Narasimha, R., Kumar, S.R., Prabhu, A. & Kailas, S.V. 2007 Turbulent flux events in a nearly neutral atmospheric boundary layer. *Phil. Trans. R. Soc. Lond. A* **365**, 841–858.
Nepf, H.M. 2012*a* Flow and transport in regions with aquatic vegetation. *Annu. Rev. Fluid Mech.* **44**, 123–142.
Nepf, H.M. 2012*b* Hydrodynamics of vegetated channels. *J. Hydraul. Res.* **50** (3), 262–279.
Nepf, H.M. & Vivoni, E.R. 2000 Flow structure in depth-limited, vegetated flow. *J. Geophys. Res. Oceans* **105** (C12), 28547–28557.
Novak, M.D., Warland, J.S., Orchansky, A.L., Ketler, R. & Green, S. 2000 Wind tunnel and field measurements of turbulent flow in forests. part i: uniformly thinned stands. *Boundary-Layer Meteorol.* **95**, 457–495.

https://doi.org/10.1017/jfm.2026.11446 Published online by Cambridge University Press

PELES, Y., KOŞAR, A., MISHRA, C., KUO, C.-J. & SCHNEIDER, B. 2005 Forced convective heat transfer across a pin fin micro heat sink. *Intl J. Heat Mass Transfer* **48** (17), 3615–3627.

PIETRI, L., PETROFF, A., AMIELH, M. & ANSELMET, F. 2009 Turbulence characteristics within sparse and dense canopies. *Environ. Fluid Mech.* **9**, 297–320.

POGGI, D., PORPORATO, A., RIDOLFI, L., ALBERTSON, J.D. & KATUL, G.G. 2004 The effect of vegetation density on canopy sub-layer turbulence. *Boundary-Layer Meteorol.* **111**, 565–587.

RAHMAN, M.A., STRATOPOULOS, L.M.F., MOSER-REISCHL, A., ZÖLCH, T., HÄBERLE, K.-H., RÖTZER, T., PRETZSCH, H. & PAULEIT, S. 2020 Traits of trees for cooling urban heat islands: a meta-analysis. *Build. Environ.* **170**, 106606.

RAUPACH, M.R., FINNIGAN, J.J. & BRUNET, Y. 1996 Coherent eddies and turbulence in vegetation canopies: the mixing-layer analogy. *Boundary-Layer Meteorol.* **78**, 351–382.

RAUPACH, M.R. & SHAW, R.H. 1982 Averaging procedures for flow within vegetation canopies. *Boundary-Layer Meteorol.* **22** (1), 79–90.

RAUPACH, M.R. & THOM, A.S. 1981 Turbulence in and above plant canopies. *Annu. Rev. Fluid Mech.* **13** (1), 97–129.

REYNOLDS, W.C. & HUSSAIN, A.K.M.F. 1972 The mechanics of an organized wave in turbulent shear flow. Part 3. Theoretical models and comparisons with experiments. *J. Fluid Mech.* **54** (2), 263–288.

SADIQUE, J., YANG, X.I.A., MENEVEAU, C. & MITTAL, R. 2017 Aerodynamic properties of rough surfaces with high aspect-ratio roughness elements: effect of aspect ratio and arrangements. *Boundary-Layer Meteorol.* **163**, 203–224.

SHARMA, A. 2020 Turbulent flows over canopies. PhD thesis, University of Cambridge, Cambridge.

SHARMA, A. & GARCÍA-MAYORAL, R. 2018 Turbulent flows over sparse canopies. *J. Phys.: Conf. Ser.* **1001**, 012012.

SHARMA, A. & GARCÍA-MAYORAL, R. 2020*a* Scaling and dynamics of turbulence over sparse canopies. *J. Fluid Mech.* **888**, A1.

SHARMA, A. & GARCÍA-MAYORAL, R. 2020*b* Turbulent flows over dense filament canopies. *J. Fluid Mech.* **888**, A2.

TAYLOR, G.I. 1938 The spectrum of turbulence. *Proc. R. Soc. Lond. A* **164** (919), 476–490.

WALLACE, J.M., ECKELMANN, H. & BRODKEY, R.S. 1972 The wall region in turbulent shear flow. *J. Fluid Mech.* **54** (1), 39–48.

WILLMARTH, W.W. & LU, S.S. 1972 Structure of the Reynolds stress near the wall. *J. Fluid Mech.* **55** (1), 65–92.

WOODING, R.A., BRADLEY, E.F. & MARSHALL, J.K. 1973 Drag due to regular arrays of roughness elements of varying geometry. *Boundary-Layer Meteorol.* **5**, 285–308.

YUE, W., MENEVEAU, C., PARLANGE, M.B., ZHU, W., HOUT, V R. & KATZ, J. 2007 A comparative quadrant analysis of turbulence in a plant canopy. *Water Resour. Res.* **43** (5), W05422.

ZHAO, T. & NEPF, H. 2024 Turbulence and bedload transport in submerged vegetation canopies. *Water Resour. Res.* **60** (12), e2024WR037694.

https://doi.org/10.1017/jfm.2026.11446 Published online by Cambridge University Press